Temperature and water vapour measurements in the framework of NDACC

Benedetto De Rosa, Paolo Di Girolamo, Donato Summa

Scuola di Ingegneria, Università degli Studi della Basilicata, Potenza, 85100, Italy

Correspondence to: Paolo Di Girolamo (paolo.digirolamo@unibas.it)

Abstract. The Raman Lidar system BASIL entered the International Network for the Detection of Atmospheric Composition Change (NDACC) in 2012. Since then measurements were carried out routinely on a weekly basis. This manuscript reports specific measurement results from this effort, with a dedicated focus on temperature and water vapour profile measurements. The main objective of this research effort is to provide a characterization of the system performance. Measurements illustrated in this manuscript demonstrate the ability of BASIL to perform measurements of the temperature profile up to 50 km and of the water vapour mixing ratio profile up to 15 km, when considering an integration time of 2 h and a vertical resolution of 150-600 m, with measurement mean accuracy, determined based on comparisons with simultaneous and co-located radiosondes, of 0.1 K and 0.1 g kg^{-1}, respectively, up to the upper troposphere. Relative humidity profiling capability up to the tropopause is also demonstrated by combining simultaneous temperature and water vapour profile measurements. Raman lidar measurements are compared with measurements from additional instruments, such as radiosondings and satellite sensors (IASI and AIRS), and with model re-analyses data (ECMWF and ECMWF-ERA). We focused our attention on four selected case studies collected during the first 2 years of operation of the system (November 2013-October 2015). Comparisons between BASIL and the different sensor/model data in terms of water vapour mixing ratio indicate biases in the altitude interval 2-15 km always within the interval ± 1 g kg^{-1} (or ± 50 %), with minimum values being observed in the comparison of BASIL vs. radisondings (± 50 % up to 15 km). Results also indicate a vertically-averaged mean mutual bias of -0.026 g kg^{-1}(or -3.8 %), 0.263 g kg^{-1} (or 30.0 %), 0.361 g kg^{-1}(or 23.5 %), -0.297 g kg^{-1} (or -25 %), -0.296 g kg^{-1} (or -29.6 %), when comparing BASIL versus radisondings, IASI, AIRS, ECMWF, ECMWF-ERA, respectively. Vertically-averaged absolute mean mutual biases are somewhat larger, i.e. 0.05 g kg^{-1}(or 16.7 %), 0.39 g kg^{-1} (or 23.0 %), 0.57 g kg^{-1}(or 23.5 %), 0.32 g kg^{-1} (or 29.6 %), 0.52 g kg^{-1} (or 53.3 %), when comparing BASIL versus radisondings, IASI, AIRS, ECMWF, ECMWF-ERA, respectively. For what concerns the comparisons in terms of temperature measurements, results indicate mutual biases in the altitude interval 3-30 km always within the interval ± 3 K, with minimum values being observed in the comparison of BASIL vs. radisondings (± 2 K within the same altitude interval). Results also reveal mutual biases within ± 3 K up to 50 km for most sensor/model pairs. Results also indicate a vertically-averaged mean mutual bias between BASIL and the radisondings, IASI, AIRS, ECMWF, ECMWF-ERA of -0.03, 0.21, 1.95, 0.14, 0.43 K, respectively. Vertically-averaged absolute mean mutual biases between BASIL and the radisondings, IASI, AIRS, ECMWF, ECMWF-ERA are 1.28, 1.30, 3.50, 1.76, 1.63 K, respectively. Based on the available dataset and benefiting from the circumstance that the

Raman lidar BASIL could be compared with all other sensor/model data, it was possible to estimate the overall bias of all sensors/datasets, this being -0.04 g kg^{-1}/0.19 K, 0.20 g kg^{-1}/0.22 K, -0.31 g kg^{-1}/-0.02 K, -0.40 g kg^{-1}/-1.76 K, 0.25 g kg^{-1}/0.04 K and 0.25 g kg^{-1}/-0.24 K for the water vapour mixing ratio/temperature profile measurements carried out by BASIL, the radisondings, IASI, AIRS, ECMWF, ECMWF-ERA, respectively.

1 Introduction

Water vapour is the most important atmospheric greenhouse gas and its increasing tropospheric concentration, though indirectly, is driven primarily by human activities. Increasing concentrations of CO_2 and CH_4, primarily associated with fossil fuel combustion, lead to warmer tropospheric temperatures, which are responsible for increased atmospheric humidity contents and ultimately lead to a warmer climate (IPCC, 2007). Water vapour in the upper troposphere/lower stratosphere (UTLS) region has a crucial role in the Earth radiative budget, and consequently in the climate system. Its presence at these altitudes being primarily associated with two main sources: transport from the troposphere, taking place mainly in the tropics, and the in-situ oxidation of methane. Temperature and water vapour concentration changes in the UTLS result in radiative forcing alterations (among others, Riese *et al*., 2012). Observations demonstrated that stratospheric water vapour concentration increases with increasing tropospheric temperature, implying the existence of a stratospheric water vapour feedback (Dessler *et al.*, 2013). The strength of this feedback has been estimated to be ~0.3 W m^{-2} K^{-1} (Dessler *et al.*, 2013). Stratospheric water vapour has also an important role in stratospheric clouds formation, which are a key element in stratospheric ozone depletion mechanisms (di Sarra *et al*., 1992, Di Girolamo *et al*., 1994). Furthermore, stratospheric water vapour has also a primary importance in the processes leading to the formation of hydrogen radicals, and consequently in stratospheric chemistry and ozone depletion mechanisms (Lossow *et al*., 2013).

Despite the well-recognized importance of having accurate tropospheric and stratospheric water vapour and temperature profile measurements, data sets of these variables and their long-term variability are limited, especially in the UTLS region. Quality water vapour measurements in the UTLS region are provided by radiosondes or balloon-borne frost-point hygrometers This latter is considered to be the most accurate water vapour sensor for the low humidity levels found in the UTLS region (Vomel *et al*., 2007). However, the global radiosonde network, including ~800 stations, is quite sparse and with limited coverage in oceanic areas. Additionally, radiosondes are quite expensive and their operational launch schedule (typically two or four times per day) use, is not sufficiently intense to guarantee the temporal resolution required for the above mentioned scientific scopes. Water vapour measurements by satellite limb sounders, both in the infrared and microwave domain, have demonstrated to lack both time and horizontal resolution (Griessbach *et al.*, 2016, Hurst *et al.*, 2014). Similar considerations apply to temperature profiling, the main source of measurements covering the upper troposphere and the stratosphere being microwave and infrared satellite sounders (Thorne *et al*., 2005).

All the above weather and climate-related issues call for highly accurate measurements of both the water vapour and temperature profiles throughout the troposphere and stratosphere, with a specific focus on the UTLS region. These motivations pushed the Network for the Detection of Atmospheric Composition Change (NDACC), formerly the

international Network for the Detection of Stratospheric Change (NCSC), to include in the early 2000s water vapour and temperature lidars among its ensemble of instruments. NDACC, originally focussing on the long-term monitoring of stratospheric changes and ozone, has progressively broadened its priorities to include the monitoring of other atmospheric species and assessing their impacts on the stratosphere and troposphere. Climate and atmospheric composition changes have a significant impact of the atmospheric thermal structure and this makes atmospheric temperature measurements of paramount importance for NDACC.

The University of BASILicata Raman Lidar system (BASIL) entered NDACC in November 2012. The primary contribution of BASIL to NDACC is to provide accurate routine measurements of the vertical profiles of both water vapour mixing ratio and temperature. Water vapour profile measurements by BASIL cover the altitude interval from surface up to ~ 15 km, while temperature profile measurements cover the altitude interval from surface up to the stratopause (~ 50 km). The possibility to measure down to the proximity of the surface is guarantee by the very compact optical design of the lidar receiver, which translates into negligible differences between the overlap functions of the two ratioed Raman signals (see details in section 4.2.1). Temperature measurements over such a wide altitude interval are possible based on the combined use of the pure rotational Raman technique (Behrendt and Reichardt, 2000), which allows covering the lowest 20 km, and the integration technique (Hauchercorne *et al*., 1992), covering the altitude region from 20 km to typically 50-55 km. The combined application of these two techniques is possible because of the presence of an overlap region (20-25 km) where both techniques properly work.

In the present research work we illustrate and discuss temperature and water vapour profile measurements from BASIL with the purpose of assessing system performance in terms of measurement BIAS. Specific measurement examples are considered for this effort, which are compared with measurements from other instruments, such as radiosondings and satellite sensors (IASI and AIRS), and with model re-analyses data (ECMWF and ECMWF-ERA).

The paper outline is as follows. Section 2 gives a brief description of the Raman lidar set-up and its operation schedule in the frame of NDACC. Section 3 describes the additional profiling sensors and model data involved in the present inter-comparison effort. Section 4 illustrates the different lidar techniques considered to measure atmospheric thermodynamic variables, while section 5 defines the statistical quantities used in the inter-comparison for the assessment of the measurement performance. Section 6 illustrates the inter-comparison results and provides an assessment of the performance of the considered sensors and models. Finally, section 7 summarizes all reported results and illustrates some possible future developments of the present study.

2 The Raman lidar BASIL and its operation in the frame of NDACC

The Network for the Detection of Atmospheric Composition Change (NDACC) became operational in 1991.It includes more than 70 globally distributed, ground-based remote-sensing research stations for the observation of the physical and chemical state of the upper troposphere and stratosphere and their changes and for assessing the impact of these changes on global climate. Trends in the chemical and physical state of the atmosphere can be detected based on the collection of long-term

databases. NDACC includes approx. 25 ground-based lidar systems distributed worldwide, which are routinely operated for the monitoring of atmospheric temperature, ozone, ozone, aerosols, water vapour and polar stratospheric clouds. To extend its research, NDACC has also established formal collaboration agreements with other eight major research networks (De Mazière *et al*., 2018), namely: the AErosol RObotic NETwork (AERONET), the Baseline Surface Radiation Network (BSRN), the Advanced Global Atmospheric Gases Experiment (AGAGE), the Global Climate Observing System (GCOS) Reference Upper-Air Network (GRUAN), the National Aeronautics and Space Administration (NASA) Micro Pulse Lidar Network (MPLNET), the Halocarbons and other Trace Species Network (HATS), the Southern Hemisphere Additional Ozonesonde Network (SHADOZ) and Total Carbon Column Observing Network (TCCON).

A fundamental aspect of NDACC is represented by the high quality standard of the collected data, which we demonstrate to be also reached by BASIL based on the results illustrated in this paper. Measurements of vertical profiles of atmospheric temperature, water vapour mixing ratio and particle backscattering coefficient at 354.7 nm from BASIL are included in the NDACC database. BASIL is the only lidar system within the network which provides simultaneous and co-located measurements of these three atmospheric variables, with the data for these three variables being ingested in the NDACC repository and made available to the NDACC community.

BASIL in located in Potenza, Italy (40°38'45" N, 15°48'29" E, elevation: 730 m). The system is located in a sea-tainer on the roof of Scuola di Ingegneria (main building) at Università degli Studi della Basilicata. The system includes a Nd:YAG laser, with both second and third harmonic generation crystals (average power: 10 W). BASIL uses a telescope in Newtonian configuration, with a 40 cm diameter primary mirror (f/1.8). The main characteristics of the lidar system are summarized in table 1. BASIL performs accurate and high-resolution measurements of atmospheric water vapour and temperature, both in daytime and night-time, based on the exploitation of the vibrational and rotational Raman lidar techniques, respectively, in the ultraviolet (Whiteman, 2003; Di Girolamo *et al*., 2009,; Behrendt and Reichardt, 2000; Di Girolamo *et al*., 2004, 2006, 2018a; Bhawar *et al*., 2011). BASIL also carries out measurements of the particle backscattering and extinction coefficient and depolarization at 354.7 nm. Relative humidity profiles are obtained from simultaneous water vapour mixing ratio and temperature profile measurements (Di Girolamo *et al.*, 2009b). A transportable version of the system, emitting two additional wavelengths (523 and 1064 nm), has been deployed in a variety of international field experiments (Bhawar *et al.*, 2008; Serio *et al.*, 2008; Wulfmeyer *et al.*, 2008; Bennett *et al.*, 2011; Ducrocq *et al.*, 2014; Macke *et al.*, 2017, Di Girolamo *et al.*, 2012a, 2012b, 2016, 2017, 2018b). BASIL was included in NDACC with the primary aim of providing water vapour mixing ratio and temperature profile measurements. Thus, a major emphasis has been put in the collection and data processing for these variables, especially for what concerns the calibration and validation efforts. In the frame of NDACC, BASIL performs routine measurements each Thursday, typically from local noon to midnight couple of hours after sun set.

Laser	Nd:YAG
Wavelengths	354.7, 532 nm
Single pulse energy	500 mJ @ 354.7 nm, 300 mJ @ 532 nm
Pulse repetition frequency	20 Hz
Beam divergence	0.5 mrad (FWHM)
Telescope	Newtonian configuration
Primary mirror diameter	0.45 m
Combined focal length	1.8 m
Field of view	0.5 mrad (FWHM)
Interference filters	Elastic, N_2, H_2O, LoJ, HiJ
Center wavelength (nm)	354.7, 532, 386.7, 407.5, 354.3, 352.9
Bandwidth (nm)	1.0, 1.0, 1.0, 0.25, 0.2, 1.0
Blocking at 354.7 nm	-, 10^{-6}, 10^{-10}, 10^{-12}, 10^{-8}1, 10^{-8}

Table 1: Main characteristics of the Raman lidar system BASIL.

In addition to a larger accuracy and vertical resolution, a further advantage of lidar techniques with respect to traditional passive remote sensors is represented by the accurate characterization of the random uncertainty affecting the measurements, which is available for altitude and each individual profile. This is determined from the signal photon number based on the application of Poisson statistics. The application of Poisson statistics to lidar signals is a correct when dealing with lidar echoes acquired both in photon-counting and analogical mode. In this latter case analogical lidar signals must first be converted into "virtual" counts. Considering an integration time of 5 min and a vertical resolution of 150 m, measurement precision at 10 km is typically 5% for water vapour mixing ratio and 1 K for temperature for night-time measurements. A detail description of the system setup has been provided in several previous publications (among others, Di Girolamo *et al*., 2009a, b).

3 Additional profiling sensors and model data involved in the inter-comparison effort

3.1 IASI

The Infrared Atmospheric Sounding Interferometer (IASI), onboard the polar orbiting MetOp satellite series, is a nadir-viewing Fourier transform spectrometer measuring the Earth atmosphere emitted radiation in the thermal infrared region (3.2-15.5 μm or 645-2760 cm^{-1}), with an apodized spectral resolution of 0.5 cm^{-1} (Siméoni et al., 1997 and Rabier et al., 2002; Collard, 2007). With at a horizontal resolution of 12 km over a swath width of 2200 km, IASI performs 14 sun-synchronous orbits with overpasses at 9:30 local time, ensuring global coverage twice per day. The main objective of IASI is to provide accurate and high resolution measurements of atmospheric temperature and humidity profiles. Temperature profiles are measured in the troposphere and stratosphere in clear-sky conditions, with an accuracy of 1 K and a vertical and horizontal resolution of 1 and 25 km, respectively, in the lower troposphere. Humidity profiles are measured in the

troposphere under cloud-free conditions, with an accuracy of 10 % and a vertical and horizontal resolution of 1-2 and 25 km, respectively. Such performance may have a major impact on many scientific areas, especially on Numerical Weather Prediction, where at present only IASI radiances are directly assimilated. IASI also provides measurements of trace gases concentrations, land and sea surface temperature and emissivity and cloud properties. For the purpose of this paper, we used the data product called IASI L2 TWT, available via EUMETCast, containing atmospheric temperature and humidity profiles at 101 pressure levels and surface skin temperature. Profiles are provided at single IASI footprint resolution, with a horizontal resolution at nadir of about 25 km. The quality of the vertical profiles retrieved in cloudy IFOVs is strongly dependent on cloud properties available in the IASI CLP product and from co-located microwave measurements.

3.2 AIRS

The Atmospheric Infrared Sounder (AIRS), launched aboard NASA's Aqua EOS satellite in 2002, is a hyper-spectral sensor including 2378 infrared channels and 4 visible/near-infrared channels, covering the spectral interval 3.7-15.4 μm (2665-650 cm^{-1}), with a spectral resolution $\lambda/\Delta\lambda$ of 1200. AIRS is operated in combination with two microwave instruments, the Advanced Microwave Sounding Unit (AMSU-A) and the Humidity Sounder for Brazil (HSB), equipped with 15 and 4 microwave channels, respectively.

The combined use of this ensemble of sensors allows to provide global coverage, accurate and high resolution measurements of atmospheric temperature and humidity profiles. Temperature profiles are measured in the troposphere and stratosphere in clear-sky conditions, with an accuracy of 1 K and a horizontal resolution of 50 km. Vertical resolution is 1 and 4 km for tropospheric and stratospheric measurements, respectively. Tropospheric humidity profiles are measured under cloud-free conditions, with a vertical resolution of 2 km and an accuracy of 15 and 50 % in lower and upper troposphere, respectively.

The Aqua satellite is located on a sun-synchronous orbit, with a nominal altitude of 705 kilometers and an orbiting period of 98.8 minutes, corresponding to ~ 14.5 orbits per day. Overpasses are at 1:30 a.m. and 1:30 p.m. local time in descending and ascending orbits, respectively. As for IASI, AIRS provides concentration measurements for a variety of trace gases. For the purpose of this paper, we used the AIRS Version 6 Level 2 Standard Retrieval Product, which is based on 6-min data averaging (Boylan *et al*., 2015).

3.4 ECMWF

Reanalysis from the European Centre for Medium-range Weather Forecasts (ECMWF) are also considered in this inter-comparison effort. Two distinct reanalysis products are considered: ERA-15 (ECMWF, 2006), covering the 15-year period from December 1978 to February 1994, hereafter referred to as ECMWF, and ERA-40 (Uppala *et al*., 2005), hereafter referred to as ECMWF-ERA40, originally intended to cover a 40-year period, but finally including a 45-year period from 1957 (International Geophysical Year) to 2002. This latter reanalysis makes use of a larger ensemble of archived data, which were not available at the time of the original analyses. Horizontal resolution of the data set is ~ 80 km, covering 60 vertical levels from surface up to 0.1 hPa. It is to be specified that IASI and AIRS data, together with a variety of additional sensors, are assimilated in ECMWF re-analyses, which makes ECMWF re-analyses partially dependent on IASI and AIRS data, with

possible non-negligible effects on the mutual biases between the satellite and the model re-analyses data. However, the mutual biases between the radiosondes and the Raman lidar, and between these two sensors and the different satellite sensors and ECMWF re-analyses are completely unaffected by sensor/model cross-dependences, as in fact radiosondes from IMAA-CNR are not assimilated by ECMWF and the Raman lidar provides completely independent measurements, which are calibrated with unassimilated radiosonde data.

4 Lidar measurements of atmospheric thermodynamic variables

4.1 Water vapour mixing ratio

Raman lidar measurements of the water vapour mixing ratio profile have been extensively reported in the literature (Whiteman *et al.*, 1992; Whiteman, 2003). The approach makes use of the roto-vibrational Raman lidar signals from water vapour and nitrogen molecules at the two Raman-shifted wavelengths λ_{H_2O} and λ_{N_2}, respectively. These signals, expressed as number of detected photons from a given altitude *z* above station level, are given by the expressions:

$$P_{H_2O}(z) = P_0 \frac{c\Delta t}{2} \frac{A_{tel}}{R^2} \eta_{H_2O} O(z)\, n_{H_2O}(z)\, \sigma_{H_2O}\, T_{\lambda_0}(z)\, T_{\lambda_{H_2O}}(z) \quad (1)$$

$$P_{N_2}(z) = P_0 \frac{c\Delta t}{2} \frac{A_{tel}}{R^2} \eta_{N_2} O(z)\, n_{N_2}(z)\, \sigma_{N_2}\, T_{\lambda_0}(z)\, T_{\lambda_{N_2}}(z) \quad (2)$$

where P_0 is the number of transmitted photons of each laser pulse at wavelength λ_0, c is the speed of light, A_{tel} is the telescope aperture area, η_{H_2O/N_2} is the overall transmitter–receiver efficiency at wavelength $\lambda_{H_2O} / \lambda_{N_2}$, Δt is the laser pulse duration, $n_{H_2O}(z) / n_{N_2}(z)$ represents the water vapour/molecular nitrogen number density, $\sigma_{H_2O} / \sigma_{H_2O}$ is the water vapour/molecular nitrogen roto-vibrational Raman cross-section, $T_{\lambda_0}(z)$ and $T_{\lambda_{H_2O}}(z) / T_{\lambda_{N_2}}(z)$ are the atmospheric transmission profiles from surface up to the scattering volume altitude z at λ_0 and $\lambda_{H_2O} / \lambda_{N_2}$, respectively. The water vapour mixing ratio profile, $x_{H_2O}(z)$, can be determined from the power ratio of $P_{H_2O}(z)$ and $P_{N_2}(z)$ through the expression:

$$x_{H_2O}(z) = K(z) \cdot \frac{P_{H_2O}(z)}{P_{N_2}(z)} \quad (3)$$

The calibration function *K(z)* is determined through a calibration procedure, which is described in detail in Di Girolamo *et al.* (2017), based on the comparison between simultaneous and co-located water vapour mixing ratio profiles from the lidar and an independent humidity sensor. For the purpose of this study, the estimate of *K(z)* is based on an extensive comparison between BASIL and the radiosonde data from the nearby station CIAO. The calibration function $K(z)=c \cdot f(z)$ includes an altitude-dependent term *f(z)* associated with the different atmospheric transmission by molecules and aerosols at the two wavelengths corresponding to the water vapour and molecular nitrogen Raman signals and with the use of narrow-band interference filters and the consequent temperature and altitude dependence of $P_{H_2O}(z)$ and $P_{N_2}(z)$ (Whiteman, 2003). *c* is the calibration constant, which is an altitude-independent term obtained from the comparison of the Raman lidar signal ratio

$P_{H_2O}(z) / P_{N_2}(z)$ and, in our specific case, the radiosondes launched from the nearby station of IMAA-CNR. While the calibration procedure applied to BASIL has been illustrated in previous papers (among others, Di Girolamo et al., 2009a,b, 2017), the sensor performance assessment purposes of the present paper impose a proper and detail description of the calibration procedure applied to BASIL before the inter-comparison effort reported in this paper. This is illustrated in section 6.1.

4.2 Temperature

In the recent past, temperature lidar measurements have become more and more important in weather and climate studies. Several lidar techniques have demonstrated to be effective for routine measurements (Behrendt, 2005). Among others, the rotational Raman technique (Behrendt and Reichardt, 2000) and the integration technique (Hauchecorne and Chanin, 1980; Hauchercorne *et al.*, 1992). The rotational Raman technique, especially if implemented in the UV, allows measuring temperature profiles typically up to the lower stratosphere, while the integration technique is successfully used to measure temperature profiles throughout the stratosphere and mesosphere.

The Raman lidar system considered in the present paper performs simultaneous temperature measurements by both the rotational Raman technique, up to approx. 25 km, and the integration technique, from 20 km up to approx. 50 km, with a partial superimposition of the two sounded ranges in the altitude interval 20-25 km and with no contamination of the elastic signals by signal-induced noise effects. To the best of our knowledge, these measurements represent the first successful demonstration of the simultaneous application in a single instrument of both the rotational Raman and integration lidar techniques in the ultraviolet spectral region, i.e. in the region where the simultaneous exploitation of these two techniques has the highest potential.

4.2.1 Rotational Raman technique

Rotational Raman lidar measurements of the atmospheric temperature profile rely on the use of the rotational Raman backscattered signals from nitrogen and oxygen molecules within two narrow spectral regions encompassing rotational lines from these two species with opposite sensitivity to temperature changes: rotational lines which are closer to the laser wavelength λ_0, characterized by lower values of the rotational quantum number J, increase in intensity with decreasing temperature, while rotational lines which are distant from the laser wavelength, characterized by higher values of J, show the opposite behavior, with their intensity increasing with increasing temperature.

Atmospheric temperature measurements are obtained from the ratio of the signal including low quantum number J rotational lines, $P_{LoJ}(z)$, over the signal including high quantum number J rotational lines, $P_{HiJ}(z)$, with centre wavelengths being λ_{LoJ} and λ_{HiJ}, respectively. Specifically, the atmospheric temperature profile, $T(z)$, is obtained from the signal ratio $R(T)= P_{HiJ}(z)/P_{LoJ}(z)$, through the inversion of the following expression:

$$R(z) = \frac{P_{HiJ}\ (z[T])}{P_{LoJ}\ (z[T])} \cong \exp\left(\frac{a}{T(z)} + b\right) \tag{4}$$

where a and b are two calibration constants, which can be determined based on the comparison of Raman lidar measurements with simultaneous and co-located temperature measurements. Thus, $T(z)$ is obtained through the analytical expression:

$$T(z) = \frac{a}{\ln R(z) - b} \tag{5}$$

In the case of BASIL, a two-parameter calibration function is well suited for the determination of the temperature profile from the $P_{LoJ}(z)$ and $P_{HiJ}(z)$ as in fact a limited number of rotational lines are selected for this purpose both in the low J and high J portions of the pure-rotational Raman spectrum (Di Girolamo *et al*., 2006). The use of a very compact optical design for the lidar receiver reduces significantly the differences between the overlap functions of the roto-vibrational Raman signals $P_{H_2O}(z)$ and $P_{N_2}(z)$ used to determine the water vapor mixing ratio profile, as well as the differences between the overlap functions of the pure-rotational Raman signals $P_{LoJ}(z)$ and $P_{HiJ}(z)$) used to determine the temperature profile. This translates into the capability for the present system to extend water vapor mixing ratio and temperature profile measurement down to the proximity of the surface, with a marginal blind region corresponding to the lowest 100-150 m.

The location of the rotational Raman signals center wavelengths λ_{LoJ} and λ_{HiJ} was determined through a specific sensitivity study accounting for the temperature sensitivity of rotational lines' intensity and the variable solar background conditions (Hammann and Behrendt, 2015). In the definition of the properties of the spectral selection devises (interference filters), λ_{LoJ} and λ_{HiJ} were selected with the purpose to guarantee comparable performance in daytime and nighttime and maximize measurement precision in the temperature range which is typically found throughout the troposphere (Di Girolamo *et al*., 2004). Based on this selection, when using an ultraviolet laser wavelength at λ_0=354.7 nm, λ_{LoJ} and λ_{HiJ} are located at 354.3 and 352.9 nm, respectively.

4.2.2 Lidar integration technique

The atmospheric number density profile, $N(z)$, can be determined from the elastic backscatter signal at wavelength λ_0, $P_{\lambda_0}(z)$, based on the application of a methodology defined by Hauchecorne and Chanin (1980). This approach assumes that aerosol and clouds contributions to $P_{\lambda_0}(z)$ are negligible, which is hypothesis verified only in unperturbed stratospheric conditions at altitudes above 25-30 km, i.e. above the background stratospheric aerosol occasionally observed in the lower stratosphere.

Once $N(z)$ is determined, the temperature profile can easily be derived. For this purpose the ideal-gas law is considered in the form:

$$p(z) = k\, N(z)\, T(z) \tag{6}$$

with $p(z)$ being the atmospheric pressure profile, $T(z)$ being the atmospheric temperature profile and k being the Boltzmann constant (1.38×10^{-23} J K^{-1}). The barometric altitude equation, also known as hydrostatic equation, is also considered:

$$\mathrm{d}p(z) = -\rho(z)\, g(z)\, \mathrm{d}z \tag{7}$$

where $\rho(z)$ is the atmospheric mass density profile and $g(z)$ is the gravitational acceleration. Equation (9) is valid under hydrostatic equilibrium conditions. The combination of equations (6) and (7) leads to the following expression (Hauchecorne and Chanin, 1980):

$$T(z) = \frac{N(z_{ref,2})}{N(z)} T(z_{ref,2}) + \frac{M}{kN(z)} \int_{z_{ref,2}}^{z} g(\varsigma) N(\varsigma) d\varsigma \tag{8}$$

where the atmospheric mass density profile has been expressed as $\rho(z) = M \times N(z)$, with M being the apparent molecular weight of atmosphere (28.97), which is considered to be constant throughout the homosphere (up to 80 km).

This algorithm can be applied starting from a reference maximum altitude, hereafter identified with the symbol $z_{ref,2}$, assuming to know the atmospheric number density and temperature values at this altitude, i.e. $N(z_{ref,2})$ and $T(z_{ref,2})$. Imposing these boundary conditions, $T(z)$ can be derived starting from the reference altitude $z_{ref,2}$ and progressively applying the algorithm down to lower levels. Temperature at an altitude $z_{ref,2+1}$, immediately below $z_{ref,2}$, can be expressed as:

$$T(z_{ref,2+1}) = \frac{N(z_{ref,2})}{N(z_{ref,2+1})} T(z_{ref,2}) + \frac{M}{kN(z_{ref,2+1})} g_{med} N_{med} \Delta z \tag{9}$$

with $\Delta z = z_{ref,2+1} - z_{ref,2}$ and g_{med} and N_{med} being the mean gravitational acceleration and atmospheric number density, respectively, between $z_{ref,2}$ and $z_{ref,2+1}$. These can be expressed as (Behrendt, 2005):

$$g_{med} = \frac{g(z_{ref,2}) + g(z_{ref,2+1})}{2} \tag{10}$$

and

$$N_{med} = \frac{N(z_{ref,2}) - N(z_{ref,2+1})}{\ln \frac{N(z_{ref,2})}{N(z_{ref,2+1})}} \tag{11}$$

The algorithm can be applied both in the downward and upward direction. Consequently the reference altitude $z_{ref,2}$ can be taken at the highest or lowest boundary level of the vertical region where the integration technique for is applied (Behrendt, 2005). However, boundary values $T(z_{ref,2})$ and $N(z_{ref,2})$ must be known with sufficiently high accuracy if temperature profiles are to be extrapolated upward because errors build up exponentially when proceeding in this direction (Behrendt, 2005). On the contrary, when an upper reference altitude is taken and the algorithm is applied downward, errors affecting $T(z_{ref,2})$ and $N(z_{ref,2})$ are not affecting the temperature profile $T(z)$ few kilometers below the reference altitude, with the systematic uncertainty affecting $T(z)$ quickly reducing (Behrendt, 2005), mainly due to the stability of the equation which limits the error propagation. This is the motivation why most lidar groups, including us, usually apply this algorithm downward, typically considering values of $T(z_{ref,2})$ and $N(z_{ref,2})$ from atmospheric climatological models or satellite data (Behrendt, 2005). Systematic errors associated with an incorrect selection of $T(z_{ref,2})$ and $N(z_{ref,2})$in the downward integration of the algorithm given in expression (9) were investigated by Leblanc *et al.* (1998), considering a value for $z_{ref,2}$=90 km and using,

as a worst-case scenario, a reference value for $T(z_{ref,2})$ exceeding by 15 K the corresponding model value at this same altitude. Leblanc *et al.* (1998) revealed that the bias was already reduced to 4 K at 80 km and to 1 K at 70 km. In real measurements, the considered value for $T(z_{ref,2})$ is expected to be much closer to its correct value. Consequently, systematic errors in the temperature profile associated with the selection of wrong temperature boundary conditions and the application of the downward-integration technique are very small (~ 1 K, Behrendt, 2005). Similar considerations are also valid for BASIL. In this case, the elastic signals extend with a sufficiently high statistics up to approx. 55 km; thus, $z_{ref,2}$ is taken equal to 55 km and boundary values $T(z_{ref,2})$ and $N(z_{ref,2})$ are taken from the mid-latitude reference atmospheric models of U.S. Standard Atmosphere (1976), considering the different seasonal options included therein (Kantor and Cole, 1962). The systematic uncertainty affecting the measurement at an altitude of 5 km below $z_{ref,2}$, i.e. at 50 km, is smaller than 1 K, as clearly highlighted by the results reported in sections 6.1 and 6.2, which reveal deviations at this altitude between BASIL and model re-analyses ECMWF and ECMWF-ERA smaller than 1 K for the case studies, i.e. considerably smaller than the statistical uncertainty affecting BASIL temperature measurements at this altitude (± 2 K). It is to be specific that only systematic errors associated with the selection of a wrong value of $T(z_{ref,2})$ are to be considered, while those associated with the selection of a wrong value of $N(z_{ref,2})$ are always negligible because deviations of real atmospheric number density profiles from climatological profiles are always very small (1-2 %) in the altitude region where boundary conditions are typically selected (50-90 km). The bias values listed above are in agreement with those reported for a variety of other Reileigh lidars operated in the frame of NDACC. Specifically, Marenco et al. (1977) reported for the Rayleigh lidar in Thule (Greenland) a potential systematic uncertainty, or bias, associated with the selection of incorrect upper boundary values smaller than the statistical uncertainty affecting the measurements (± 2 K). These results were obtained based on a dedicated sensitivity analysis, with upper boundary values varied by 5 %. Leblanc et al. (1998b) reported bias values from a variety of temperature lidar systems based on Rayleigh technique included in NDACC. Specifically, temperature measurements from the CNRS-SA Rayleigh lidars at Observatoire de Haute Provence (France) and at the Centre d'Essais des Landes were found to be characterized by a bias smaller than 1 K at 55 km, while those from the NASA-Jet Propulsion Laboratory Rayleigh lidars located at Table Mountain (California) and at Mauna Loa (Hawaii) were characterized by a bias smaller than 1 K at 55 and 50 km, respectively. A bias of ~1 and ~2 K, again associated with the selection of incorrect upper boundary values, was found to characterize the Rayleigh lidars located at Hohenpeissenberg (Germany) and Sondre Stromfjord (Greenland), respectively (Dou et al., 2009).

4.3 Relative humidity

The availability of simultaneous and co-located measurements of the water vapour mixing ratio and temperature profiles, as is the case for BASIL, makes the determination of the relative humidity profile straightforward. Relative humidity is defined as the ratio, expressed in percentage, between the water vapour partial pressure profile $e(z)$ and the saturated vapor pressure profile $e_{sat}(z)$, i.e. $RH(z) = 100 \times e(z)/e_{sat}(z)$. $e(z)$ can be expressed as:

$$e(z) = \frac{p(z)x_{H_2O}(z)}{0.622 + x_{H_2O}(z)} \tag{12}$$

with $p(z)$ being the atmospheric pressure profile, usually taken from simultaneous measurements with other sensors (for example radiosondes) or obtained from surface pressure measurements, assuming hydrostatic equilibrium and applying the hydrostatic equilibrium equation. A commonly used expression for $e_{sat}(z)$ (List, 1951) is given by:

$$e_s(z) = 6.108 \exp\left\{\frac{17.08\left[T(z) - 273.15\right]}{T(z) - 38.97}\right\} \tag{13}$$

with $T(z)$ being expressed in degrees Celsius. As $e_{sat}(z)$ depends only on $T(z)$, $RH(z)$ can be determined from BASIL measurements of $x_{H_2O}(z)$ and $T(z)$, based on the only knowledge of the surface pressure value.

5 Statistical quantities used for the inter-comparison

In order to assess the performance of the different profiling sensors and models considered in the study, an appropriate statistical analysis has to be carried out based on the estimation of specific statistical quantities. Specifically, for each sensor/model pair, the percentage bias and root-mean square deviation profile between two profiles, can be determined through the following expressions (Behrendt *et al*., 2007a, 2007b, Bhawar *et al*., 2011):

$$BIAS = \frac{1}{N}\sum_{i=1}^{N} BIAS_i = \frac{2}{N}\sum_{i=1}^{N}\left\{\frac{\sum_{z=z_1}^{z_2}\left[q_1(z) - q_2(z)\right]}{\sum_{z=z_1}^{z_2}\left[q_1(z) + q_2(z)\right]}\right\} \tag{14}$$

$$RMS = \frac{1}{N}\sum_{i=1}^{N} RMS_i = \frac{2}{N}\sum_{i=1}^{N}\left\{\frac{\sqrt{N\sum_{z=z_1}^{z_2}\left[q_1(z) - q_2(z)\right]^2}}{\sum_{z=z_1}^{z_2}\left[q_1(z) + q_2(z)\right]}\right\} \tag{15}$$

where $q_1(z)$ where $q_2(z)$ represent the water vapor mixing ratio or temperature values at altitude z for sensor/model 1 and sensor/model 2, respectively, z_1 and z_2 are the lower and upper levels of the considered altitude interval, respectively, and N is the number of data points for each sensor/model in this interval. In the expressions above we used the mean of the measurement result of the two sensors/models as reference instead of using the measurement result of one of the two. This approach leads to more objective results than considering one of the sensors/models as reference (Behrendt *et al.* (2007a,b).

For all inter-comparisons reported in this paper, bias and RMS deviation are computed in the 500 m altitude intervals (z_2-z_1=500 m). The index i, having values in the range from 1 to N, identify the inter-comparison sample, where N is the total number of possible comparisons for each sensor/model pair. Profiles of mean bias and RMS deviation are finally computed taking into consideration the total number of possible inter-comparisons for each sensor/model pair. For the purpose of applying expressions (14) and (15) we considered a common altitude array for each pair of sensors. Consequently, in case of

different altitude arrays for the compared profiles, data from one sensor/model have to be interpolated to the other sensor/model altitude levels. A linear interpolation is used in the present effort for the water vapour mixing ratio and temperature data. The bias and root-mean-square deviation can be determined from expressions (14) and (15), respectively, through their multiplication by the mean of the two profiles:

$$\frac{2\sum_{z=z_1}^{z_2}\{q_1(z)+q_2(z)\}}{N} \quad (16)$$

The estimate of the bias and root-mean square deviation between two compared sensors/models allows quantifying the mutual performance of the two , i.e. how one performances with respect to the other. The bias, which quantifies the relative accuracy of the compared sensors/models, identifies an offset between the two, which is attributable to different sources of systematic uncertainty affecting one or both sensors/models. As opposed to this, the root-mean-square deviation includes all possible differences between the two sensors/models, associated with both systematic and statistical uncertainties and with changes of the measured/modeled atmospheric parameter (water vapour mixing ratio or temperature) as a result of differences in the considered air masses. Based on expressions (14) and (16), the bias and percentage bias of the sensor/model 1 vs. the sensor/model 2 has positive values when $q_1(z)$ is larger than $q_2(z)$, i.e. $q_1(z)$ overestimates $q_2(z)$ or $q_2(z)$ overestimates $q_1(z)$.

6 Inter-comparison results

BASIL was approved to enter NDACC in November 2012 and started operations shortly afterwards. However, routine measurements on a weekly basis started only one year later. In this paper we report measurements performed during the two year period from 7 November 2013 to 5 October 2015. During this time interval BASIL collected 385 hours of measurements distributed over 80 days. Lidar measurements are compared with model re-analyses (ECMWF, ECMWF-ERA40), satellite data (IASI, AIRS), and radiosondes from CNR in Tito. Figure 1 shows the location of BASIL (Lat: 40,60 °N, Long.: 14,85 °E), together with the footprint of AIRS (centered at Lat: 40,50 °N and Long: 15,50 °E, size: 72×72 km) and IASI (centered at Lat: 40,89 °N and Long: 16,02 °E, size: 12×12 km) and the size of grid point of ECMWF ERA-15 and ECMWF ERA-40 (centered at Lat: 40,63 °N and Long: 15,75 °E size: 9×9 km). The distance between BASIL and the center point of the other sensors/models is variable, i.e. 8 km with CIAO radiosonde launching facility at IMAA-CNR, 25 km with AIRS, 25 km with IASI and 4 km with ECMWF ERA-15 and ECMWF ERA-40.

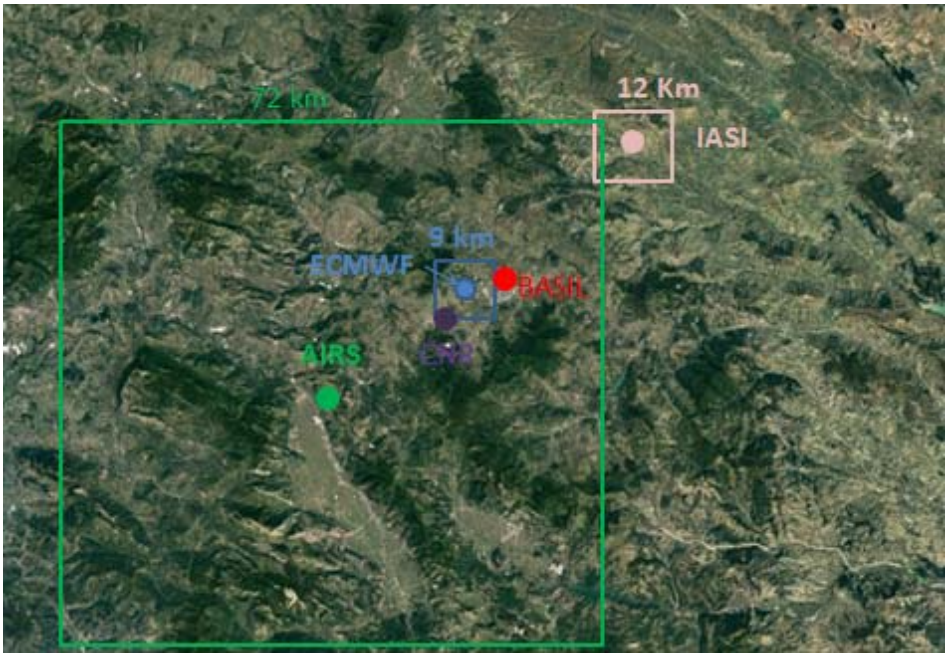

Figure 1: Location of BASIL (red dot), together with the footprint of AIRS (green square centered on green dot) and IASI (pink square centered on pink dot), CIAO radiosonde launching facility (purple dot) and the grid point of ECMWF ERA-15 and ECMWF ERA-40 (blue square centered on blue dot).

For the aims of this paper, we focused our attention on six selected case studies collected during the first 2 years of operation of the system, namely 7 November 2013, 19 December 2013, 9 October 2014, 27 November 2014, and 2 and 9 April 2015. While a larger data-set could have been chosen, we decided to focus our attention only on clear sky cases. In fact, clear sky condition represents the most suited condition for both water vapour and temperature measurements by Raman lidar, with water vapour profile measurements extending up to the UTLS region and temperature profile measurements extending up to 50 km. An appropriate assessment of measurement performance based on a sensors/models inter-comparison effort requires the sensors to be operated in clear sky conditions, which is not always the case for either the Raman lidar or the two passive space sensors IASI and AIRS. More specifically, the Raman lidar system BASIL does not have an all-weather measurement capability, which implies that the system is shut down in case of precipitation. Additionally, BASIL - and this is true for all lidar systems - cannot penetrate thick clouds, the laser beam being completely extinguished for optical thicknesses around 2. Acceptable Raman lidar performance are still possible above thin clouds, with optical thickness < 0.3. Thus, for the purposes of the present inter-comparison effort, even the presence of high cirrus clouds makes case studies non eligible for the comparison. In other case studies IASI and/or AIRS data were characterized by a very poor quality and unrealistic biases, which forced us to remove those from the inter-comparison effort. After April 2015, the laser experienced a period of

reduced emitted power, possibly as a results of an unidentified internal optical misalignment. This determined a detriment of the lidar performance, which prevented from considering these measurements within this inter-comparison effort.

6.1 Raman lidar calibration

The Raman lidar has been calibrated based on an extensive comparison with the radiosondes launched from the nearby station of IMAA-CNR, which is only 8.2 km away from the Raman lidar. Launched radiosondes are manufactured by Vaisala (model: RS92-SGP). For the purpose of determining the calibration constant *c* the Raman lidar and radiosonde profiles are compared over the altitude interval 2.5-4 km, i.e. above the boundary layer. In fact, in clear sky conditions, the horizontal homogeneity of the humidity field above the boundary layer top is sufficiently high to allow assuming that the Raman lidar and the radiosonde are sounding the same air masses. Within this altitude interval, Raman lidar signals are strong and characterized by high signal-to-noise ratios and small statistical uncertainties. At the same time, within this low level altitude interval, the horizontal drift of the radiosonde with respect to the vertical of lidar station is limited, so that again the two sensors can be actually assumed to be sounding the same air masses. The calibration constant *c* is obtained through a best-fit procedure applied to the Raman lidar and radiosonde data, the value of the constant being determined by minimizing the root mean square deviation between the single data points from the two profiles within the altitude interval 2.5-4 km. As the Raman lidar and the radiosonde data have different altitude arrays, for the purpose of applying the best-fit algorithm, radiosonde data have been interpolated to the Raman lidar altitude levels.

For the purpose of determining the calibration constant *c*, a specific inter-comparison effort between BASIL and the radiosondes launched from IMAA-CNR was carried out in the period 9 October 2014-7 May 2015. An overall number of 11 comparisons, including all coincident measurements, were possible. In this respect, it is to be specified that routine radiosonde launches started at IMAA-CNR only on October 2014, so inter-comparisons before this date were very infrequent. Figure 2 illustrates the vertical profiles of the water vapour mixing ratio and temperature mean BIAS and RMS deviation for the 11 considered comparisons. The altitude interval 2.5-4 km was used to quantify the mean value of the calibration constant, $\overline{c}$, which is obtained by averaging the single calibration coefficient values from all 11 inter-comparisons. The uncertainty affecting the calibration constant, σ_c, has been estimated as the standard deviation all single calibration values from the mean value. The value of $\overline{c}$ is found to be equal to 82.33, while the value of σ_c is found to be equal to 3.72. The standard deviation, expressed in percentage ($100 \times \sigma_c,/\overline{c}$), is found to be equal to 4.5 %. A very similar procedure was applied to calibrate temperature measurements. In this case the mean value and standard deviation of the calibration constants *a* and *b* were determined, with $\overline{a} \pm \sigma_a$= 760 ± 7 and $\overline{b} \pm \sigma_b$=0.97 ± 0.03.

The constancy of the calibration constant was verified over the two years measurement period, appearing quite stable, as in fact neither short-term or long-term time variations were revealed. Ageing of transmitter/receiver components does not produce any appreciable variation of the calibration coefficients.

For what concerns water vapour mixing ratio measurements, above the planetary boundary layer and up to 8.5 km (figure 2a), the mean BIAS is found to not exceeding ± 0,25 g/kg (or ± 10 %). Even at high altitudes (figure 2b) bias values are very

low as in fact above 8.5 km this is not exceeding ± 0,06 g/kg (or ± 50 %). For what concerns the temperature measurements, above the planetary boundary layer and up to 9.5 km, biases are within ± 1 K.

The above specified uncertainties affecting water vapour measurements are in agreement with those reported for a variety of other Raman lidars operated in the frame of NDACC. Specifically, Whiteman et al. (2012) reported a 5% uncertainty in the upper troposphere based on an extended comparison of the NASA-GSFC Raman lidar system ALVICE with Vaisala RS92 radiosondes. For the Maïdo Lidar in Réunion island Dionisi et al. (2015) reported a relative difference below 10 % in the low and middle troposphere (2–10 km) based on the comparison with 15 co-located and simultaneous Vaisala RS92 radiosondes. The upper troposphere, up to 15 km, is found to be characterized by a larger spread (approximately 20 %), attributed to the increasing distance between the two sensors. Leblanc et al. (2012) reported water vapor mixing ratio profiles measurements from the JPL Raman lidar at Table Mountain Facility (California) with a demonstrated capability of covering from ~1 km above ground to the lower stratosphere with a precision better than 10 % below an altitude of 13 km, with an estimated accuracy of 5 %. The same authors also reported a very good agreement between the Raman lidar and a Cryogenic Frost-Point Hygrometer in the entire lidar range 3–20 km, with a mean bias not exceeding 2% (lidar dry) in the lower troposphere and 3% (lidar moist) in the UTLS.

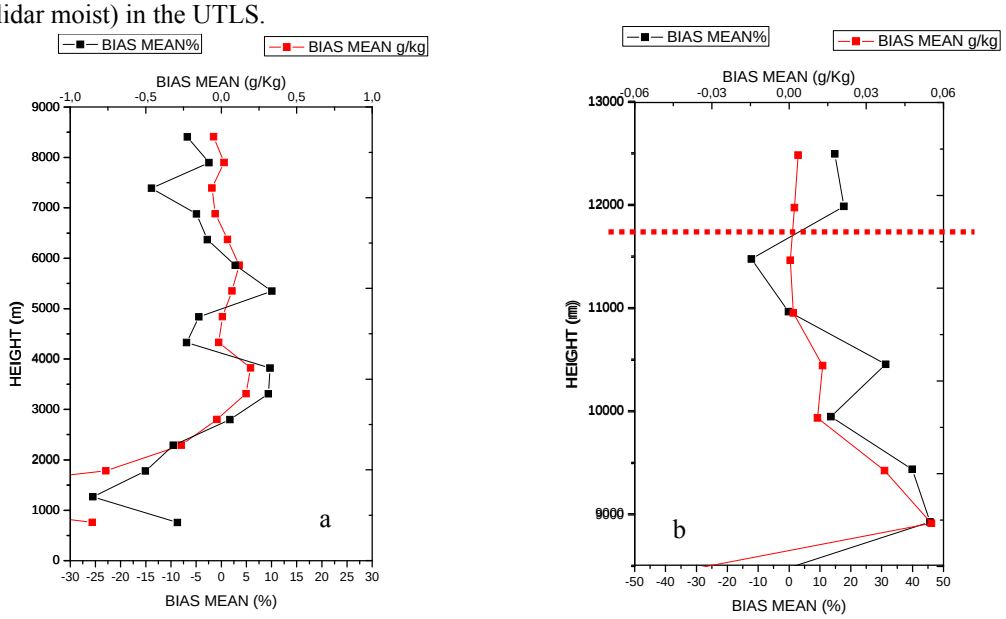

Fig. 2: Vertical profiles of water vapour mixing ratio mean BIAS and RMS deviation for the 11 comparisons of BASIL vs. the radiosondes available in the the period 9 October 2014- 7 May 2015: (a) water vapour mixing ratio: vertical interval 0-8.5 km; (b) water vapour mixing ratio: vertical interval 8.5-13 km. The dashed red line in panel b represents the mean tropopause altitude.

6.2 Case studies

Figure 3a illustrates the mean water vapour mixing ratio profile measured by BASIL on 7 November 2013 over the time interval 17:00-19:00 UTC. The vertical resolution of the data is 150 m from surface up to 6 km, 300 m between 6 and 8 km

and 600 m above 8 km. The water vapour mixing ratio profile from BASIL reaches an altitude of approx. 15 km, with the capability to measure humidity levels as small as 0.003-0.004 g kg^{-1}, with a sensitivity level of 0.001-0.002 g kg^{-1}, the two levels being defined as the mixing ratio values corresponding to 50 and 100 % relative uncertainty in the UTLS region. The capability to reach an altitude of 14-15 km, with a measurement detection level of 0.001-0.002 g kg^{-1}, has been verified in most of the 2 h water vapour profiles measured by BASIL in the frame of NDACC in clear sky conditions. When considering measurements integrated in time over the entire night, the water vapour mixing ratio profile by BASIL is found to extend up to approx. 16-18 km. For this case study, the closest in time water vapour mixing ratio profiles from IASI (at 19:20 UTC) and AIRS (at 14:09 U.T.C.) and the model re-analysis ECMWF ERA-15 and ECMWF ERA-40 (at 18:00 UTC) are also illustrated in figure 3a. In the present case study, no radiosonde was launched from the nearby CIAO launching station. The agreement between BASIL and the different sensors/models is very good, even at low altitudes where effects of water vapour heterogeneity are usually important. For this specific case study, at all altitudes above 2.5 up to 15 km, deviations of BASIL vs. AIRS and IASI are smaller than 0.2 g kg^{-1} (or 40 %) and 0.1 g kg^{-1} (or 30 %), respectively, while deviations between BASIL and ECMWF (ERA-15 and ERA-40) are not exceeding 0.1 g kg^{-1} (or 30 %). The mean bias of BASIL vs. AIRS, IASI, ECMWF and ECMWF -ERA40 are -16 % (or -0.13 g kg^{-1}), 7% (or 0.08 g kg^{-1}), -5% (or 0.0032g kg^{-1}) and -11% (or -0.05 g kg^{-1}), respectively. For this case study, IASI and AIRS properly reproduce over a large portion of the sounded interval the water vapour mixing ratio profile observed by BASIL, but fail in correctly reproducing the mixing ratio values observed in the ABL. This missing capability of IASI and AIRS to properly reproduce water vapour structures within the boundary layer had already been reported by Chazette et al. (2014), based on an extensive comparison of Raman lidar and IASI profile measurements carried out in the frame of the HyMeX and ChArMEx programs, attributing it to the weighting functions of IASI not correctly sampling layers close to the ground.

Figure 3b shows the time evolution of the water vapour mixing ratio over a 6 h time interval from 16:00 to 22:00 UTC on this same day (7 November 2013). The figure is a succession of 72 consecutive 5-min averaged profiles. For the purpose of reducing signal statistical fluctuations, a vertical smoothing filter was applied to the data, finally achieving an overall vertical resolution of 150 m. The considered vertical smoothing filter is a simple central moving or running average computed using equally spaced data (vertical step=30 m) on either side of the point where the mean is calculated, which requires using an odd number of data points in the filter window. Figure 3b reveals the presence of a well-defined humid layer extending from surface up to ~1.5 km between 16:00 and 17:00 UTC and then progressively reducing in depth down to 2-300 m, which identifies the evolution of the convective boundary-layer in its final decaying phase at the solar portion of the day. A variety of humidity layers are visible above, with humidity values as large as 2 g kg^{-1} up to 4 km. The ability to perform water vapour mixing ratio profile measurements with such high time resolution is a unique feature of Raman lidars.

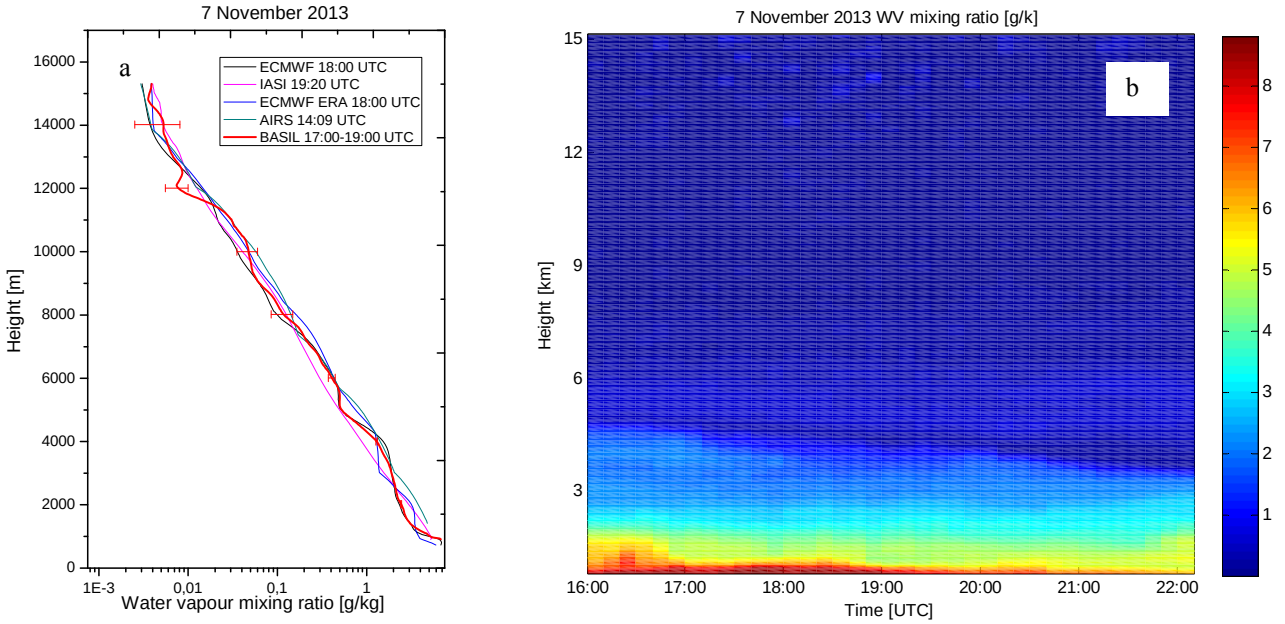

Figure 3: Water vapour mixing ratio profile as measured by BASIL over the time period 17:00-19:00 UTC on 7 November 2013, together with the closest in time profiles from IASI (at 19:29 UTC), AIRS (at 14:09 UTC) and the model re-analysis ECMWF (ERA-15 and ERA-40, at 18:00 UTC) (panel a). Time evolution of water vapour mixing ratio profile as measured by BASIL over the interval 16:00-22:00 UTC on 7 November 2013 (panel b).

Figure 4a illustrates the mean atmospheric temperature profile measured by BASIL on 7 November 2013 over the same time interval considered in figure 3a. The measurement is based on the use of the rotational technique up to 20 km and the integration technique above 20 km. The combined use of these two techniques allows temperature profile measurements up to 50-55 km. In the altitude region exploited through the rotational Raman technique the vertical resolution is 150 m from surface up to 6 km and 600 m above this altitude. The integration technique is applied downward, initializing the algorithm at an altitude of 55 km. As mentioned above, although the boundary value of $T(z_{ref,2})$ taken from a model atmosphere may differ from its real value, the systematic error affecting the measurement becomes negligible 5-7.5 km below this level (Hauchercorne *et al.*, 1992). For this motivation, profiles in figure 4a and b are shown only below 50 km.

Again, the closest in time temperature profiles from the sensors IASI (at 19:20 UTC) and AIRS (at 14:09 UTC) and the model re-analysis ECMWF and ECMWF-ERA40 (at 18:00 UTC) are also illustrated in figure 4a. The agreement between BASIL and the different sensors/models is very good. Specifically, deviations between BASIL and AIRS/IASI are smaller than 2 K from surface up to 40 km and smaller than 3-5 K above. Deviations between BASIL and ECMWF analysis (ERA-15 and ERA-40) are not exceeding 2 K all the way up to 50 km. It is to be pointed out that deviations between BASIL and the other sensors/models may be the results of the random and systematic uncertainties affecting the different sensors, as well as of the different air masses sounded by the different sensors or encompassed in the different grid points. However, it is to be added that temperature measurements by lidar frequently reveal temperature fluctuations associated with the

propagation of internal gravity waves (Di Girolamo *et al.*, 2009a). These fluctuations, having amplitudes increasing with increasing altitude, can be as large as 5-15 K (Chanin *et al.*, 1994; Zhao *et al.*, 2017). Consequently, deviations between BASIL and the other sensors/models are in part possibly associated with the effects of gravity waves. The mean bias of BASIL vs. AIRS, IASI, ECMWF and ECMWF-ERA40 are 1.05 K, 0.83 K, 0.41 K and -0.72K, respectively.

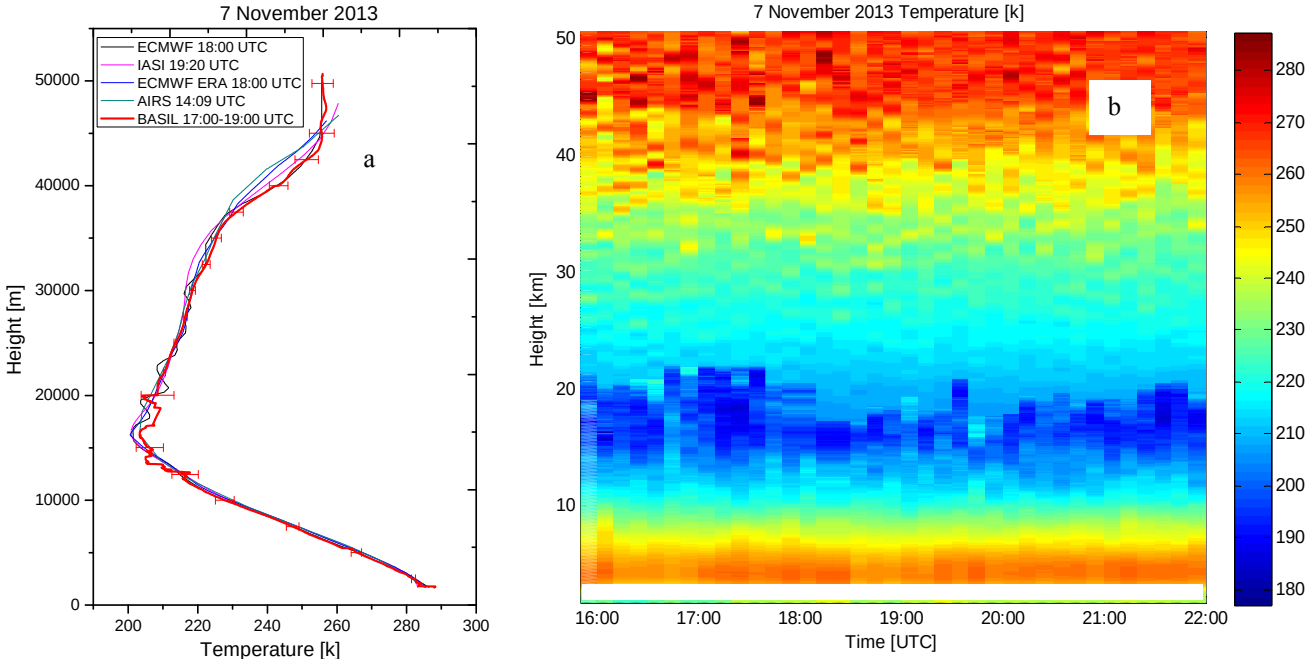

Figure 4: Vertical profile of atmospheric temperature as measured by BASIL over the time period 17:00-19:00 UTC on 7 November 2013, together with the closest in time profiles from IASI (at 19:20 UTC), AIRS (at 14:09 UTC) and the model re-analysis ECMWF (ERA-15 and ERA-40, at 18:00 UTC) (panel a). Time evolution of atmospheric temperature as measured by BASIL over the interval 18:00-22:00 UTC on 7 November 2013 (panel b).

Figure 4b shows the evolution of atmospheric temperature over the same 6 h time interval considered in figure 3b. Again, the figure is a succession of 72 consecutive 5-min averaged profiles. In this case, for the purpose of obtaining a sufficiently high signal statistics, a vertical resolution of 150 m was considered. It is to be noticed that, despite the short integration time, the strong signal intensities, in combination with favourable clear weather conditions, allows reaching an altitude of 50 km. The tropopause region and its fluctuations are clearly visible in the figure.

Accurate relative humidity (RH) measurements are of paramount importance to determine cloud and aerosol radiative properties and related microphysical processes. RH has been demonstrated to have a critical influence on aerosol climate forcing (Pilins *et al.*, 1995). Aerosol hygroscopic growth at high relative humidity values may significantly influence aerosol direct effect on climate (Wulfmeyer and Feingold, 2000). As described in section 4.3, RH profiles are obtained from the simultaneous and independent measurements of the water vapour mixing ratio and temperature profiles carried out by BASIL. Figure 5a illustrates the mean atmospheric relative humidity profile measured by BASIL on 7 November 2013 over

the same time period considered in figures 3a and 4a. The agreement between BASIL and the different sensors/models is good, with deviations not exceeding 10 % up to 15 km.

Figure 5b shows the time evolution of relative humidity over the same 6 h interval considered in figures 3b and 4b, the present figure being again a succession of 72 consecutive 5-min averaged profiles with a vertical resolution of 150 m. It is to be noticed that, despite the short integration time, an altitude of 15 km is reached, with measurements revealing a RH variability in the UTLS region systematically larger than the random uncertainty affecting the Raman lidar measurements.

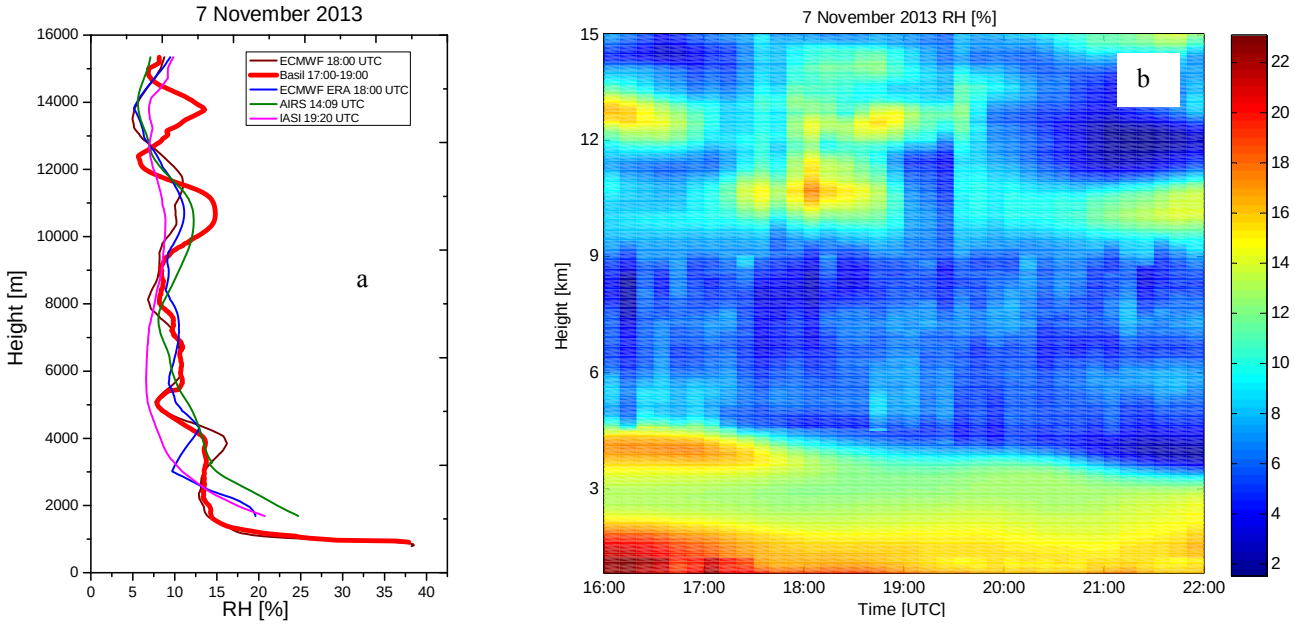

Figure 5: Vertical profile of relative humidity as measured by BASIL over the time period 17:00-19:00 UTC on 7 November 2013, together with the closest in time profiles from IASI (at 19:20 UTC), AIRS (at 14:09 UTC) and the model re-analysis ECMWF (ERA-15 and ERA-40, at 18:00 UTC) (panel a). Time evolution of relative humidity as measured by BASIL over the interval 18:00-22:00 UTC on 7 November 2013 (panel b).

6.3 Assessment of the BIAS and RMS deviation between the different sensors/models

The performance of the different profiling sensors and models considered in the present study are assessed through a dedicated statistical analysis. Specifically, for each sensor/model pair and each case study, the relative bias and root-mean square (RMS) deviation profiles are determined in terms of both water vapour mixing ratio and temperature.

The overall number of all possible sensor/model pairs is 15, which is the maximum number of pairs possible when 5 sensors/models are available. More specifically, these are BASIL vs. radisondings (RS), BASIL vs. IASI, BASIL vs. AIRS, BASIL vs. ECMWF, BASIL vs. ECMWF-ERA, RS vs. IASI, RS vs. AIRS, RS vs. ECMWF, RS vs. ECMWF-ERA, IASI vs. AIRS, IASI vs. ECMWF, IASI vs. ECMWF-ERA, AIRS vs. ECMWF, AIRS vs. ECMWF-ERA and ECMWF vs. ECMWF-ERA. For each sensor/model pair we are considering 6 comparisons, one for each of the considered case studies (7 November 2013, 19 December 2013, 9 October 2014, 27 November 2014, and 2 and 9 April 2015). The considered time

interval is always the closest in time to the 2 hour integration interval considered for the Raman lidar. Table 2 lists the time intervals for all sensors7models for all considered case studies.

Case study	BASIL	RS	IASI	AIRS	ECMWF and ECMWF-ERA
7 November 2013	17:00-19:00	/	18:08	14:09	18:00
19 December 2013	16:00-18:00	18:00	19:19	/	18:00
9 October 2014	16:00-18:00	18:00	19:20	14:35	18:00
27 November 2014	18:00-20:00	18:00	18:14	14:33	18:00
2 April 2015	18:00-20:00	18:29	18:59	15:18	18:00
9 April 2015	18:00-20:00	18:35	19:08	15:32	18:00

Table 2: Time intervals for all sensors7models for all considered case studies.

For all inter-comparisons reported in this paper, we computed bias and RMS deviation considering vertical intervals of 500 m (i.e. z_2-z_1= in expressions (14) and (15) is taken equal to 500 m). Considering equally spaced data points with a vertical step of 30 m, the statistical analysis to compute the bias and RMS deviation is applied over 17 data points. The upper level of the comparison may vary for each different sensor/model pair and may vary from day-to-day.

Figure 6 shows the water vapour mixing ratio BIAS and RMS deviation profiles for all sensor/model pairs. As expected, the BIAS shows larger values in the ABL (in the range -3/+5 g kg^{-1}), with values being typically smaller than ±1 g kg^{-1} above 2 km. More specifically, in the ABL the BIAS of BASIL vs. the radiosondes is in the range ±0.3 g kg^{-1}, with similar small values being also observed in the comparison of BASIL vs. ECMWF-ERA40. Larger BIAS values in the ABL are found to characterize the comparisons of BASIL/radisondes/ECMWF-ERA40 vs. IASI and AIRS, with values up to 5 g kg^{-1}. In this regard, it is to be pointed out that, while the distance between BASIL and the radiosonde launching facility (IMAA-CNR) is only ~7 km and the grid point of ECMWF ERA-15 and ECMWF ERA-40 has a size of 9×9 km, is centered in between BASIL and IMAA-CNR and includes both sites, the distance between BASIL and IASI/AIRS footprint centers is ~25 km, these footprints having sizes of 12×12 km and 72×72 km, respectively. Consequently, when comparing BASIL/radisondes/ECMWF-ERA40 vs. IASI and AIRS, the effects associated with water vapour heterogeneity are more important (see figure 1).

For all sensor/model pairs, the BIAS shows values smaller than ±0.1 g kg^{-1} above 8 km and smaller than ±0.02 g kg^{-1} above 10 km. In the altitude region 8-16 km the mutual bias of BASIL vs. the radiosondes or ECMWF is smaller than ±0.01 g kg^{-1}, while above 10 km the mutual bias of BASIL vs. ECMWF-ERA40 and AIRS vs. IASI is smaller than ±0.07 g kg^{-1}. The mutual bias of BASIL vs. AIRS or IASI is in the range smaller than 0.01 g kg^{-1} above 11 km. RMS deviation values are comparable with BIAS values for all sensor/model pairs, which testifies that statistical uncertainties and changes in the measured/modeled atmospheric parameters poorly contribute to profiles' deviations. More specifically, for all sensor/model

pairs, the RMS deviation shows values smaller than ±1.5 g kg^{-1} above 2 km, smaller than ±0.1 g kg^{-1} above 8 km and smaller than ±0.02 g kg^{-1} above 10 km.

For all sensor/model pairs, the percentage BIAS shows values in the range ±60 % all the way up to 16 km. The smallest percentage bias is found in the comparison of BASIL vs. the radiosondes, with values not exceeding ±18 % all the way up to 12 km and values in the range ±13 % above the ABL and up to 4 km. A small percentage bias is also found in the comparison of BASIL vs. ECMWF, with values not exceeding ±30 %. Positive percentage bias values in the range 0-60 % are found to characterize the comparison of BASIL/radisondes/ECMWF-ERA40 vs. IASI and AIRS at all altitudes, which testifies that IASI and AIRS underestimate all other sensors/models. Percentage bias values in the range ±25 % are found in the comparison of IASI vs. AIRS in the altitude region 6-16 km, while larger values (up to 50 %) are found below 6 km, the agreement between the two sensors in the upper portion of the profile confirming that they both are underestimating all other considered sensors/models (BASIL/radisondes/ECMWF-ERA). Values of the percentage RMS deviation for the comparison of BASIL vs. the radiosondes and ECMWF are smaller than 40 % up to 11 km and smaller than 30 % above. Values of the percentage RMS deviation typically smaller than 50 %, but with sporadic values as large as 65-70 %, are found to characterize the comparison of BASIL/radiosondes/ECMWF-ERA vs. IASI and AIRS at all altitudes.

Figure 7 illustrates the temperature BIAS and RMS deviation profiles for all sensor/model pairs. The BIAS of BASIL vs. the radiosondes is in the range ±1 K above the ABL up to 12 km, with deviations in the ABL not exceeding 2 K.

Except for a few points, BIAS values are within ±2 K up to 30 km, this being the maximum altitude typically reached by the radiosondes. The BIAS of BASIL vs. ECMWF-ERA40 is within the range ±0.8 K up to 12.5 km. For all sensor/model pairs, the BIAS shows values in the range ±5 K all the way up to 50 km. As for the water vapour mixing ratio, RMS deviation values for all sensor/model pairs are slightly exceeding BIAS values, which testifies the limited contribution of statistical uncertainties and changes in the measured/modeled atmospheric parameters in determining the deviations between profile pairs.

So far we have reported and discussed the mutual bias and RMS deviation profiles between different sensors/models, highlighting the altitude variability of these quantities. However, in order to assess sensors and models performance is often preferable to use a single bias/RMS deviation value. This leads us to the definition of the vertically-averaged mean bias and the vertically-averaged mean bias.

The vertically-averaged mean bias, $\overline{bias}$, and RMS deviation, $\overline{RMS}$, over the entire inter-comparison range is determined through the application of the weighted mean (Bhawar *et al.*, 2011):

$$\overline{bias} / \overline{RMS} = \frac{\sum_{i=1}^{N} w_i \left(bias_i / RMS_i \right)}{\sum_{i=1}^{N} w_i} \tag{17}$$

where $bias_i/RMS_i$ being the mean bias/RMS within the ith vertical interval, w_i is the corresponding weight and N is the number of vertical windows (each having a vertical extent of 500 m, see section 5). N may vary for the different

sensor/model pairs. For the comparisons in terms of water vapour mixing ratio, which extends up to 16 km, the number of vertical windows N is equal to 30. The comparisons in terms of temperature extends up to 50 km for all different sensor/model pairs, with the number of vertical windows N being equal to 98, with the only exception of the comparisons including the radiosondes, in this case the number of vertical windows N being typically equal to 58.

The weight w_i is given by the number of inter-comparisons possible within each vertical window and varies between 0 and 6, this latter value representing the total number of case studies included in this inter-comparisons effort. A weighted mean is necessary because, in case of missing data at some specific altitude, the number of inter-comparisons may be smaller than 6 and thus data from these altitudes must have a lower weight in the vertically-averaged mean.

The vertically-averaged absolute mean bias, $\overline{|bias|}$, and RMS deviation, $\overline{|RMS|}$, defined as the weighted mean of the moduli of the single bias values at different altitudes, can be determined through the expression:

$$\overline{|bias/RMS|} = \frac{\sum_{i=1}^{N} w_i |bias_i/RMS_i|}{\sum_{i=1}^{N} w_i} \quad (18)$$

In the vertically-averaged absolute mean bias $\overline{|bias|}$, values at different altitudes with different signs will not cancel out. Consequently, values of $\overline{|bias|}$ are larger than the corresponding $\overline{bias}$ values.

Table 3 includes the vertically-averaged mean mutual bias, $\overline{bias}$, and RMS deviation, $\overline{RMS}$, values and the vertically-averaged absolute mean mutual bias values, $\overline{|bias|}$, for the water vapour mixing ratio inter-comparison, which includes all possible sensor/model pairs. The smallest $\overline{bias}$ value is found to characterize the comparison of radiosondes vs. BASIL (0.0246 g kg^{-1}). Small values of the $\overline{bias}$ are also found in the comparison of ECMWF and ECMWF-ERA40 vs. IASI and AIRS (ECMWF vs. IASI=-0.0295 g kg^{-1}, ECMWF vs. AIRS=-0.042 g kg^{-1}, ECMWF-ERA40 vs. IASI= 0.053 kg^{-1}, ECMWF-ERA40 vs. AIRS= 0,086 g kg^{-1}). As a possible motivation behind these low values it is to be considered that ECMWF reanalysis products, as those used in the present inter-comparison effort (ECMWF ERA 15 and ERA 40), heavily rely on the assimilation of IASI and AIRS data, especially in the UTLS region. This aspect is also responsible for the small $\overline{bias}$ value of ECMWF vs. ECMWF ERA (-0.056 g kg^{-1}). Larger $\overline{bias}$ values are found to characterize the comparison of BASIL/radiosondes vs. IASI, AIRS, ECMWF and ECMWF-ERA40. For what concerns the vertically-averaged absolute mean bias, $\overline{|bias|}$,values are somewhat larger than those of $\overline{bias}$. Specifically, the value of $\overline{|bias|}$ for the comparison of radiosondes vs. BASIL is 0.05 g kg^{-1}. Relatively small values of the $\overline{|bias|}$ are also found in the comparison of ECMWF and ECMWF-ERA40 vs. IASI and AIRS (ECMWF vs. IASI=0.16 g kg^{-1}, ECMWF vs. AIRS=0.29 g kg^{-1}, ECMWF-ERA40 vs. IASI= 0.41 kg^{-1}, ECMWF-ERA40 vs. AIRS= 0.27 g kg^{-1}).

The value of $\overline{RMS}$ for the comparison of radiosondes vs. BASIL is 0.135 g kg^{-1}, which is sensitively larger than the corresponding $\overline{bias}$ values. This is most probably the effect of the large statistical uncertainty affecting BASIL measurements in the UTLS region and the radiosonde horizontal drift, which determines humidity profile changes which are associated with different sounded air-masses. Large $\overline{RMS}$ values are also found to characterize the comparison of AIRS vs.

all other sensors/models (AIRS vs. BASIL=0.446 g kg^{-1}, AIRS vs. CNR= 0.687 g kg^{-1}, AIRS vs. IASI=0.381 g kg^{-1}, AIRS vs. ECMWF=0.33 g kg^{-1}, AIRS vs. ECMWF-ERA40=0.216 g kg^{-1}). The motivation for these large values is the large size of AIRS footprint (72×72 km), which determines a measurement loss of representativeness when compared to all other localized sensor/model data. Large values of $\overline{RMS}$ are also found to characterize the comparison of IASI vs. all other sensors/models (IASI vs. BASIL=0.302 g kg^{-1}, IASI vs. RS= 0.63 g kg^{-1}, IASI vs. ECMWF=0.165 g kg^{-1}, IASI vs. ECMWF-ERA40=0.252 g kg^{-1}). Such large values are possibly associated with the considerable distance between IASI footprint and all other sensors and models, especially in the presence of horizontal heterogeneities in the humidity field. The large $\overline{RMS}$ values characterizing the comparisons of BASIL/radiosondes vs. ECMWF/ECMWF-ERA40 are again possibly associated with the limited effectiveness of these re-analyses within the ABL, where most humidity is located, as well as with their poor effectiveness in the UTLS region.

Values of the percentage $\overline{bias}$ confirm most of the considerations above. It is to be pointed out that the percentage $\overline{bias}$ is a quantity very sensitive to the variability of the data in the UTLS region, more than the $\overline{bias}$, as in fact the water vapour mixing ratio has a large variability within the troposphere, varying over four orders of magnitude from the surface to the UTLS region. A very small percentage $\overline{bias}$ value is found to characterize the comparison of radiosondes vs. BASIL (3.84%), this value being in good agreement with the $\overline{bias}$ value and testifying the accuracy and agreement of these two sensors throughout the sounded vertical interval, especially in the ABL and in the UTLS. Small values of the percentage $\overline{bias}$ are also found to characterize the comparison of ECMWF vs. IASI/AIRS (ECMWF vs. IASI= -2.26 %, ECMWF vs. AIRS=-2.19 %). Relatively small values of $\overline{|bias|}$ are also found to characterize the comparison of radiosondes vs. BASIL (16.7 %) and the comparison of ECMWF vs. IASI/AIRS (ECMWF vs. IASI=30.56 %, ECMWF vs. AIRS=29.6 %).

Table 4 includes the vertically-averaged mean mutual bias and RMS deviation values, $\overline{bias}$ and $\overline{RMS}$, and the vertically-averaged absolute mean mutual bias values, $\overline{|bias|}$, for the temperature inter-comparison for all considered sensor/model pairs. It is to be specified that, while an estimate of the percentage bias and RMS deviation is necessary for the adequate assessment of quality (accuracy/precision) of the water vapour mixing ratio measurements/analyses, as in fact this quantity may vary more than four orders of magnitude in the altitude interval considered in this inter-comparison effort (0-16 km), there is no need for an estimate of the percentage bias and RMS deviation characterizing temperature measurements/analyses, which is a quantity characterized by a much smaller variability (not exceeding 30 %) in the considered interval (0-50 km), with the largest values at surface (typically 280-300 K) and the smallest values at the tropopause (typically 200-210 K). The smallest $\overline{bias}$ values characterize the comparison of radiosondes vs. BASIL (0.03 K) and ECMWF-ERA40 vs. IASI (-0.14 K). Small $\overline{bias}$ values are also found in the comparison of ECMWF vs. BASIL (-0.14 K), BASIL vs. ECMWF-ERA40 (0.43 K), BASIL vs. IASI (0.21 K), RS vs. ECMWF (0.57 K), ECMWF-ERA40 vs. RS (0.28 K) and RS vs. IASI (0.51 K). Additional small $\overline{bias}$ values are also found to characterize the comparison of ECMWF

vs. ECMWF-ERA40 (0.58 K) and ECMWF vs. IASI (0.65 K). Larger $\overline{bias}$ values are found to characterize the comparison of AIRS with all other sensors/models (BASIL vs. AIRS = 1.95 K, RS vs. AIRS =0.89, AIRS vs. IASI=-1.33 K, ECMWF vs. AIRS=2.14 K and ECMWF-ERA40 vs. AIRS =1,19 K), with AIRS always underestimating all other sensors and models. The above results reveal, with the only exception of AIRS, a very good agreement between all sensors and a remarkable capability of the considered models to reproduce the measured temperature profiles. As clearly shown by the bias profiles in figure 7a, most part of the bias between AIRS and all other sensors/models is found above 37 km, which reveal a negative systematic uncertainty affecting AIRS temperature profile measurements above this altitude (AIRS underestimating all other sensors/models) up to 5 K. Part of this bias is also to be attributed to the fact that AIRS slightly underestimates all other sensors/models around the tropopause. Additionally, the small bias characterizing the comparisons of IASI with all other sensors/models testify the very good performance of this sensor in terms of temperature profile measurements and its correct assimilation in ECMWF analyses. With a few exceptions, values of $\overline{|bias|}$ are in the range 1-2 K. A low value of the $\overline{RMS}$ deviation characterize the comparison of BASIL vs. the radiosondes (1.86 K). This low value is to be attributed to the fact that the comparison between BASIL and the radiosondes only extends up to 30 km and consequently the effects associated with the large statistical fluctuations affecting BASIL signals in the 30-50 km region, with the sounding of different air-masses and with gravity waves propagation are sensitively reduced. Relatively small $\overline{RMS}$ values are also found in the comparison of ECMWF/ECMWF-ERA40 vs. IASI (1.88 K and 1.83 K, respectively).

6.4 Overall bias affecting all sensors/models

Making use of the available statistics of comparison results, an approach is considered to determine the overall bias values for all sensors/models involved in this inter-comparison effort. This approach, originally proposed by Behrendt *et al.* (2007a,b), can be applied in case there is at least one sensor whose measurements are comparable with all other sensors/models. For this purpose we considered the Raman lidar BASIL. Assuming equal weight on the data reliability of each sensor/model, an estimate of the overall bias affecting all sensors/models is obtained by imposing that the summation of all mutual biases between sensor/model pairs is equal to zero. The choice of attributing equal weight to the data reliability of each sensor/model is driven by the awareness that none of them can *a priori* be assumed more accurate than the others and thus by the assumption that the closest profile to a reference profile can be obtained by taking the mean of all available profiles. Based on this approach, the overall bias affecting water vapour profile data from BASIL, the radiosondes, IASI, AIRS, ECMWF and ECMWF-ERA40 is estimated to be -0.04 g kg^{-1}, 0.20 g kg^{-1}, -0.31 g kg^{-1}, -0.40 g kg^{-1}, 0.25 g kg^{-1} and 0.25 g kg^{-1}, respectively, as sketched in figure 8a.

The same approach was applied to determine the overall temperature bias for all sensors/models involved in this inter-comparison effort. In this case, as we have previously identified a significant systematic uncertainty affecting AIRS measurements, this sensor was excluded from the summation of all mutual biases between sensor/model pairs. Thus, assuming equal weight on the data reliability of all other sensor/model the overall bias affecting temperature profile data from BASIL, the radiosondes, IASI, AIRS, ECMWF and ECMWF-ERA40 is found to be 0.19 K, 0.22 K, -0.02 K, -1.76 K,

0.04 K and -0.24 K, respectively, as sketched in figure 8b. These results confirm that AIRS systematically underestimates all other sensors and models.

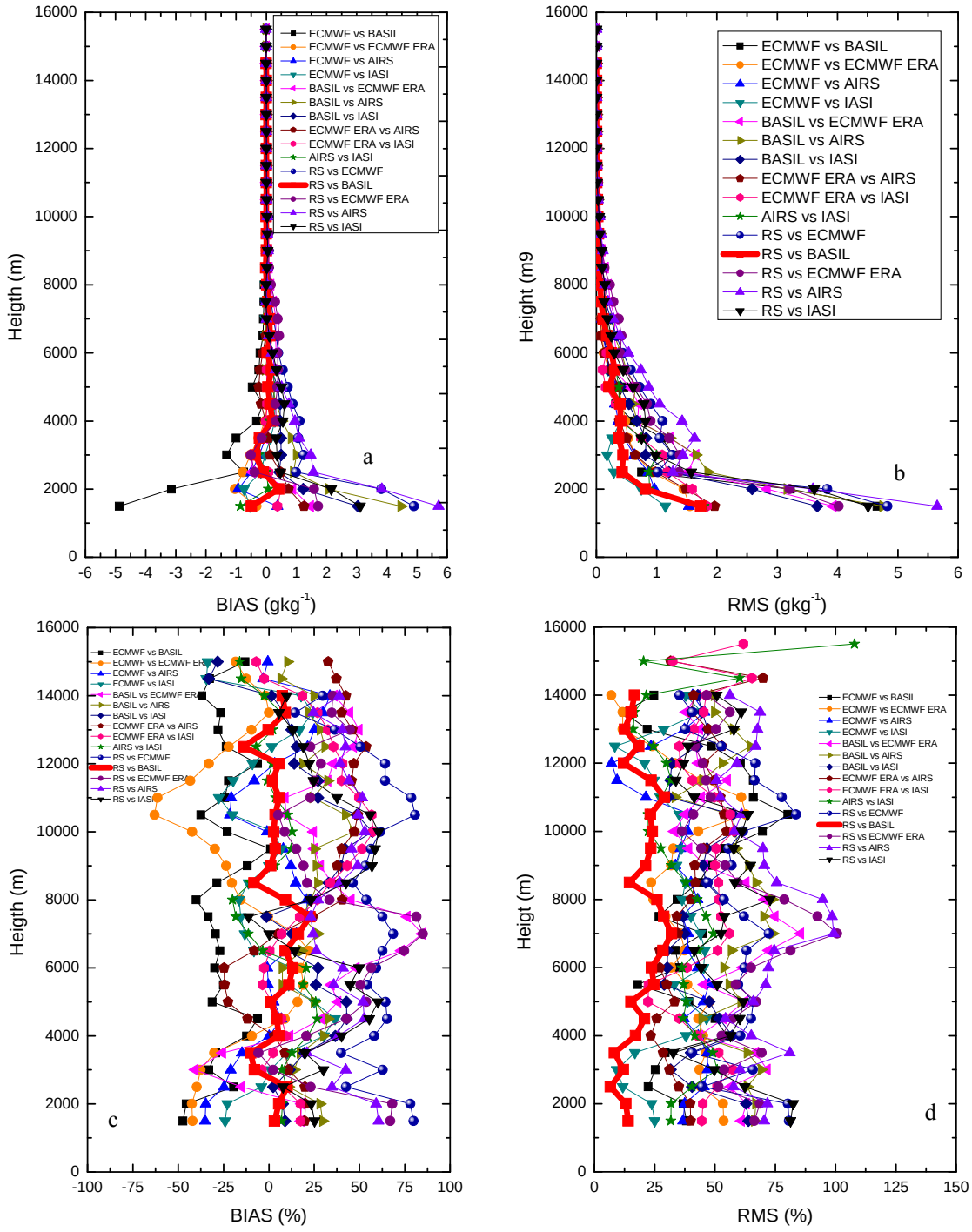

Figure 6: Vertical profiles of water vapour mixing ratio mean BIAS and RMS deviation for all sensor/model pairs: (a) BIAS, RMS (b) percentage BIAS (c) and percentage RMS (d).

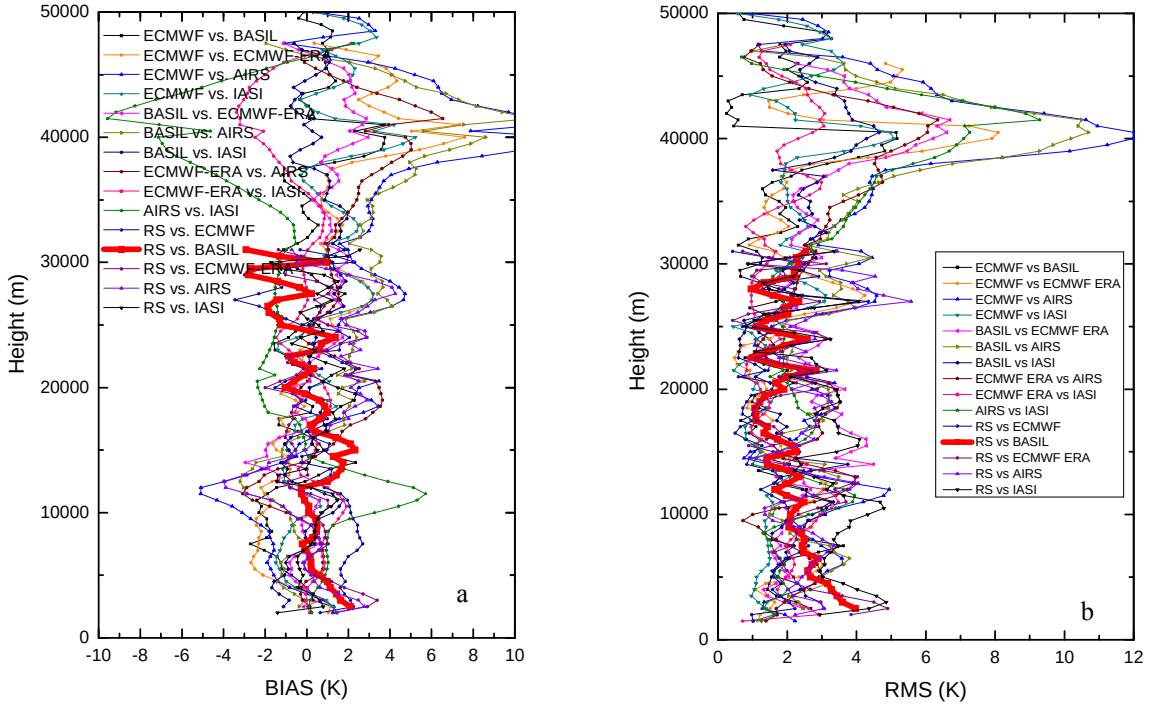

Figure 7: Vertical profiles of temperature mean BIAS and RMS deviation for all sensor/model pairs: (a) BIAS, RMS (b).

	RS vs. ECMWF ERA	**ECMWF ERA vs. AIRS**	**ECMWF ERA vs. IASI**	**RS vs. AIRS**	**RS vs IASI**	**AIRS vs IASI**	**ECMWF vs ECMWF ERA**	**ECMWF vs AIRS**	**ECMWF vs IASI**	**BASIL vs ECMWF ERA**	**RS vs BASIL**	**BASIL vs AIRS**	**BASIL vs IASI**	**ECMWF vs BASIL**	**RS vs ECMWF**
$\overline{bias}$ **(g kg^{-1})**	0.241	0.086	0.053	0.577	0.306	0,031	-0.056	-0.042	-0.0295	-0.296	0.0246	0.361	0.263	0.297	0.300
$\overline{\lvert bias \rvert}$ (g kg^{-1})	0.69	0.27	0.41	0.72	0.63	0,22	0,16	0,29	0,16	0,32	0,05	0,57	0,39	0,32	0.48
$\overline{RMS}$ **(g kg^{-1})**	0,579	0,216	0,252	0,687	0,63	0.381	0,159	0,33	0,165	0,543	0,135	0,446	0,302	0,324	0,343
$\overline{bias}$ **(%)**	34,8	23,065	22,767	40,625	30,39	6.86	-16,56	-2,19	-2,257	-29,63	3,84	23,46	22,96	25,03	55,43
$\overline{\lvert bias \rvert}$(%)	50,96	39,42	45,33	67.45	52,67	33,55	35,43	40,25	30,56	28.43	16,68	54,49	41,42	29,6	56,80
$\overline{RMS}$ **(%)**	58,66	39,94	45,47	68,975	54,97	37,25	35,6	40,76	31,77	52,20	19,40	58,49	43,76	30,93	58,23

Table 3: Water vapour mixing ratio vertically-averaged mean and absolute mean BIAS and RMS deviation values for all considered sensor/model pairs.

	ECMWF ERA vs. RS	ECMWF ERA vs. AIRS	ECMWF ERA vs. IASI	RS vs. AIRS	RS vs IASI	AIRS vs IASI	ECMWF vs ECMWF ERA	ECMWF vs AIRS	ECMWF vs IASI	BASIL vs ECMWF ERA	RS vs BASIL	BASIL vs AIRS	BASIL vs IASI	ECMWF vs BASIL	RS vs ECMWF
$\overline{bias}$ (K)	0.28	1.19	-0.14	0.89	0.51	-1.33	0.58	2.14	0.65	0.43	0.03	1.95	0.21	-0.14	0.57
$\overline{\lvert bias \rvert}$ (K)	1.33	2.77	1.21	2.15	1.17	3.06	2.14	3.82	1.84	1.63	1.28	3.50	1.30	1.76	1.55
$\overline{RMS}$ (K)	2.,19	2.82	1.83	2.73	3.01	3.11	2.45	3.86	1.88	2.96	1.86	4.56	2.31	3.24	1.63

Table 4: Temperature vertically-averaged mean and absolute mean BIAS and RMS deviation values for all considered sensor/model pairs.

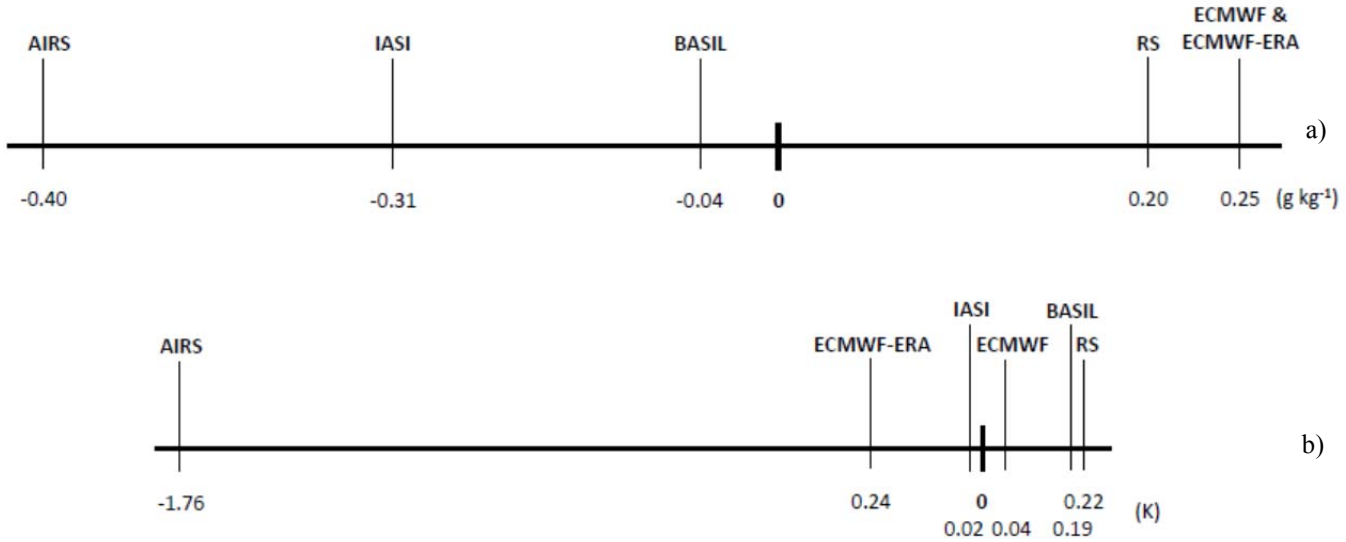

Figure 8: Overall bias affecting water vapour profile (a) and temperature (b) data**.**

7 Summary

Case studies illustrated in this paper demonstrate the ability of BASIL to perform temperature profile measurements up to 50 km and water vapour mixing ratio profile measurements up to 15 km, considering an integration time of 2 hours and a vertical resolution of 150-600 m, with a measurement accuracyof 0.1 K and 0.1 g kg^{-1}, respectively. Temperature and water vapour profile measurements carried out by BASIL are compared with profiles from a variety of other sensors/models, namely radiosondings, the satellite instruments IASI and AIRS and the model re-analyses data (ECMWF and ECMWF-ERA). Comparisons between BASIL and the different sensor/model data in terms of water vapour mixing ratio indicate a vertically-averaged mean mutual bias of -0.026 g kg^{-1}(or -3.8 %), 0.263 g kg^{-1} (or 30.0 %), 0.361 g kg^{-1}(or 23.5 %), -0.297 g kg^{-1} (or -25 %), -0.296 g kg^{-1} (or -29.6 %), when compared with radisondings, IASI, AIRS, ECMWF, ECMWF-ERA, respectively. Vertically-averaged absolute mean mutual biases are somewhat larger, i.e. 0.05 g kg^{-1}(or 16.7 %), 0.39 g kg^{-1} (or 23.0 %), 0.57 g kg^{-1}(or 23.5 %), 0.32 g kg^{-1} (or 29.6 %), 0.52 g kg^{-1} (or 53.3 %), when comparing BASIL versus

radisondings, IASI, AIRS, ECMWF, ECMWF-ERA, respectively. Comparisons in terms of temperature measurements reveal a mean/absolute mean mutual bias between BASIL and the radisondings, IASI, AIRS, ECMWF, ECMWF-ERA of -0.03/1.28, 0.21/1.30, 1.95/3.50, 0.14/1.76 and 0.43/1.63 K, respectively. Larger temperature biased are found between AIRS and all other sensors/models, which is the result of AIRS slightly underestimating all other sensors/models around the tropopause and above 37 km.

The possibility to assess the overall bias values for all sensors/models included in this inter-comparison effort was also exploited, benefiting from the circumstance that the Raman lidar BASIL could be compared with all other sensor/model data. The overall bias affecting water vapour/temperature profile data from BASIL, the radiosondes, IASI, AIRS, ECMWF and ECMWF-ERA40 was estimated to be -0.04 g kg^{-1}/0.19 K, 0.20 g kg^{-1}/0.22 K, -0.31 g kg^{-1}/-0.02 K, -0.40 g kg^{-1}/-1.76 K, 0.25 g kg^{-1}/0.04 K and 0.25 g kg^{-1}/-0.24 K.

The present study allows us to get confidence on the high quality of the water vapour and temperature profiling carried out by BASIL and included in the NDACC database and on the possibility to use long-term records of these measurements for monitoring of atmospheric composition and thermal structure changes and, ultimately, for climate trend studies.

Author contribution

Paolo Di Girolamo designed the experiment and together with Benedetto De Rosa and Donato Summa carried out the measurements. Benedetto De Rosa and Donato Summa developed the data analysis algorithms and the former of the two carried out the data analysis. Benedetto De Rosa and Paolo Di Girolamo prepared the manuscript with contributions from Donato Summa.

Acknowledgements

This work was possible based on the support from the Italian Ministry for Education, University and Research under the Grant OT4CLIMA.We thank GCOS Reference Upper-Air Network (GRUAN) for the provision of the radiosonde data. I specific thank is given to IMAA-CNR of Tito Scalo and the site representative Dr. Fabio Madonna. ECMWF data used in this study have been obtained from the ECMWF Data Server (https://apps.ecmwf.int/datasets/data/interim-full-daily/levtype=sfc/). IASI Level-2 wter vapor mixing ratio and temperature profiles used in this paper are taken from EUMESAT database (https://eoportal.eumetsat.int/userMgmt/protected/welcome.faces), while AIRS data are obtained from the NASA Goddard Earth Sciences Data Information and Services Center (GESDISC).

References

Bennett, L. J., Blyth, A. M., Burton, R. R., Gadian, A. M., Weckwerth, T. M., Behrendt, A., Di Girolamo, P., Dorninger, M., Lock, S.-J., Smith, V. H., Mobbs, S. D.: Initiation of convection over the Black Forest mountains during COPS IOP15a. Quarterly Journal of the Royal Meteorological Society, 137, 176-189, ISSN: 0035-9009, doi: 10.1002/qj.760, 2011.

Bhawar, R., Bianchini, G., Bozzo, A., Cacciani, M., Calvello, M.R., Carlotti, M., Castagnoli, F., Cuomo, V., Di Girolamo, P., Di Iorio, T., Di Liberto, L., di Sarra, A., Esposito, F., Fiocco, G., Fua, D., Grieco, G., Maestri, T., Masiello, G., Muscari, G., Palchetti, L., Papandrea, E., Pavese, G., Restieri, R., Rizzi, R., Romano, F., Serio, C., Summa, D., Todini, G., Tosi, E.: Spectrally Resolved Observations of Atmospheric Emitted Radiance in the H_2O Rotation Band, Geophysical Research Letters, 35, L04812, ISSN: 0094-8276, doi: 10.1029/2007GL032207, 2008.

Bhawar, R., P. Di Girolamo, D. Summa, C. Flamant, D. Althausen, A. Behrendt, C. Kiemle, P. Bosser, M. Cacciani, C. Champollion, T. Di Iorio, R. Engelmann, C. Herold, Müller, D., S. Pal, M. Wirth, V. Wulfmeyer: The Water Vapour Intercomparison Effort in the Framework of the Convective and Orographically-Induced Precipitation Study: Airborne-to-Ground-based and airborne-to-airborne Lidar Systems, Q. J. Roy. Meteor. Soc., 137, 325–348, 2011.

Behrendt, A., and Reichardt, J.: Atmospheric temperature profiling in the presence of clouds with a pure rotational Raman lidar by use of an interference-filter-based polychromator, Appl. Opt., 39, 1372–1378, 2000.

Behrendt, A Temperature measurements whth lidar in: Lidar Range-Resolved Optical Remote Sensing of the Atmosphere, edited by: Weitkamp, C., Springer, New York, 2005.

Behrendt, A.,Wulfmeyer, V., Di Girolamo, P., Kiemle, C., Bauer, H-S., Schaberl, T., Summa, D., Whiteman, D. N., Demoz, B. B., Browell, E. V., Ismail, S., Ferrare, R., Kooi, S., Ehret, G.,,Wang, J.: Intercomparison of water vapor data measured with lidar during IHOP 2002. Part I: Airborne to ground-based lidar systems and comparisons with chilled-mirror hygrometer radiosondes. J. Atmos. Oceanic Technol., 24, 3–21, 2007a.

Behrendt, A.,Wulfmeyer, V., Kiemle, C., Ehret, G., Flamant, C., Schaberl, T., Bauer, H-S., Kooi, S., Ismail, S., Ferrare, R., Browell, E. V., Whiteman, D. N.: Intercomparison of water vapor data measured with lidar during IHOP 2002. Part II: Airborne-to-airborne systems. J. Atmos. Oceanic. Technol. 24, 22–39, 2007b.

Boylan, P., J. Wang, S. A. Cohn, E. Fetzer, E. S. Maddy, and S. Wong: Validation of AIRS Version 6 Temperature Profiles and Surface-Based Inversions over Antarctica using Concordiasi Dropsonde Data, Journal of Geophysical Research: Atmospheres, 992-1007, 120, doi:10.1002/ 2014JD022551, 2015.

Chanin, M. L., Hauchercorne, A., Garnier, A., and D. Nedeljkovic, D.: Recent lidar developments to monitor stratosphere-troposphere exchange, Journul o/Afmmphrric and 7-erresrrid Phyms, Vol.56 . No. 9. pp. 1073-1081, 1994.

Chazette, P., F. Marnas, J. Totems, and X. Shang, Comparison of IASI water vapor retrieval with H2O-Raman lidar in the framework of the Mediterranean HyMeX and ChArMEx programs, Atmos. Chem. Phys., 14, 9583–9596, doi:10.5194/acp-14-9583-2014, 2014.

Collard, A. D.: Selection of IASI channels for use in numerical weather prediction, J. R. Meteorol. Soc. 133: 1977–1991, DOI: 10.1002/qj.178, 2007.

De Mazière, M., Thompson, A. M., Kurylo, M. J., Wild, J. D., Bernhard, G., Blumenstock, T., Braathen, G. O., Hannigan, J. W., Lambert, J.-C., Leblanc, T., McGee, T. J., Nedoluha, G., Petropavlovskikh, I., Seckmeyer, G., Simon, P. C., Steinbrecht, W., and Strahan, S. E.: The Network for the Detection of Atmospheric Composition Change (NDACC): history, status and perspectives, Atmos. Chem. Phys., 18, 4935-4964, https://doi.org/10.5194/acp-18-4935-2018, 2018.

Dessler, A. E., Schoeberl, M. R., Wang, T., Davis, S. M., and Rosenlof, K. H.: Stratospheric water vapor feedback, P. Natl. Acad. Sci. USA, 110, 18087–18091, doi:10.1073/pnas.1310344110, 2013.

Di Girolamo, P., Cacciani, M., di Sarra, A., Fiocco, G., Fuà, D.: Lidar observations of the Pinatubo aerosol layer at Thule, Greenland, Geophys. Res. Lett., 21, 1295-1298, doi: 10.1029/93GL02892, 1994.

Di Girolamo, P., Marchese, R., Whiteman, D. N., Demoz, B. B.: Rotational Raman Lidar measurements of atmospheric temperature in the UV, Geophys. Res. Lett., 31, doi: 10.1029/2003GL018342, 2004.

Di Girolamo, P., Behrendt, A., Wulfmeyer, V.: Spaceborne profiling of atmospheric temperature and particle extinction with pure rotational Raman lidar and of relative humidity in combination with differential absorption lidar: performance simulations, Appl. Opt., 45, 2474-2494, doi:10.1364/AO.45.002474, 2006.

Di Girolamo, P.,, Summa, D., Ferretti, R.: Multiparameter Raman Lidar Measurements for the Characterization of a Dry Stratospheric Intrusion Event. J. Atmos. Oceanic Technol., 26, 1742-1762, doi: 10.1175/2009JTECHA1253.1, 2009a.

Di Girolamo, P., Summa, D., Lin, R.-F., Maestri, T., Rizzi, R., Masiello, G.: UV Raman Lidar measurements of relative humidity for the characterization of cirrus cloud microphysical properties, Atmos. Chem. Phys., 9, 8799-8811, doi: 10.5194/acp-9-8799-2009, 2009b.

Di Girolamo, P., Summa, D., Bhawar, R., Di Iorio, T., Cacciani, M., Veselovskii, I., Dubovik, O., and Kolgotin, A.: Raman Lidar observations of a Saharan dust outbreak event: Characterization of the dust optical properties and determination of particle size and microphysical parameters, Atmos. Environ., 50, 66–78, https://doi.org/10.1016/j.atmosenv.2011.12.061, 2012a.

Di Girolamo, P., Summa, D., Cacciani, M., Norton, E. G., Peters, G., and Dufournet, Y.: Lidar and radar measurements of the melting layer: observations of dark and bright band phenomena, Atmos. Chem. Phys., 12, 4143–4157, https://doi.org/10.5194/acp-12-4143-2012, 2012b.

Di Girolamo, P., Flamant, C., Cacciani, M., Richard, E., Ducrocq, V., Summa, D., Stelitano, D., Fourrié, N., and Saïd, F.: Observation of low-level wind reversals in the Gulf of Lion area and their impact on the water vapour variability, Q. J. Roy. Meteor. Soc., 142, 153–172, https://doi.org/10.1002/qj.2767, 2016.

Di Girolamo, P., Cacciani, M., Summa, D., Scoccione, A., De Rosa, B., Behrendt, A., and Wulfmeyer, V.: Characterisation of boundary layer turbulent processes by the Raman lidar BASIL in the frame of HD(CP)2 Observational Prototype Experiment, Atmos. Chem. Phys., 17, 745–767, https://doi.org/10.5194/acp-17-745-2017, 2017.

Di Girolamo, P., Behrendt, A., Wulfmeyer, V.: Space-borne profiling of atmospheric thermodynamic variables with Raman lidar: performance simulations, Optics Express, 26(7), 7955-7964 , https://doi.org/10.1364/OE.26.008125, 2018a.

Di Girolamo, P., Scoccione, A., Cacciani, M., Summa, D., De Rosa, B., and Schween, J. H.: Clear-air lidar dark band, Atmos. Chem. Phys., 18, 4885-4896, https://doi.org/10.5194/acp-18-4885-2018, 2018b.

Dionisi, D., Keckhut, P., Courcoux, Y., Hauchecorne, A., Porteneuve, J., Baray, J. L., Leclair de Bellevue, J., Vérèmes, H., Gabarrot, F., Payen, G., Decoupes, R., and Cammas, J. P.: Water vapor observations up to the lower stratosphere through the Raman lidar during the Maïdo Lidar Calibration Campaign, Atmos. Meas. Tech., 8, 1425–1445, https://doi.org/10.5194/amt-8-1425-2015, 2015.

di Sarra, A, Cacciani, M., Di Girolamo, P., Fiocco, G., Fuà, D., Knudsen, B., Larsen, N., Joergensen, T. S.: Observations of correlated behaviour of stratospheric ozone and aerosol at Thule during winter 1991-1992, Geophys. Res. Lett., vol. 19, p. 1823-1826, ISSN: 0094-8276, doi: 10.1029/92GL01887, 1992.

Dou, Xiankang, Tao Li, Jiyao Xu, Han-Li Liu, Xianghui Xue, Shui Wang, Thierry Leblanc, I. Stuart McDermid, Alain Hauchecorne, Philippe Keckhut, Hassan Bencherif, Craig Heinselman, Wolfgang Steinbrecht, M. G. Mlynczak, and J. M. Russell IIISeasonal oscillations of middle atmosphere temperature observed by Rayleigh lidars and their comparisons with TIMED/SABER observations, Journal of Geophysical Research, 114, D20103, doi:10.1029/2008JD011654, 2009.

Ducrocq, V., I. Braud, S. Davolio, R. Ferretti, C. Flamant, A. Jansa, N. Kalthoff, E. Richard, I. Taupier-Letage, P. Ayral, S. Belamari, A. Berne, M. Borga, B. Boudevillain, O. Bock, J. Boichard, M. Bouin, O. Bousquet, C. Bouvier, J. Chiggiato, D. Cimini, U. Corsmeier, L. Coppola, P. Cocquerez, E. Defer, J. Delanoë, P. Di Girolamo, A. Doerenbecher, P. Drobinski, Y. Dufournet, N. Fourrié, J.J. Gourley, L. Labatut, D. Lambert, J. Le Coz, F.S. Marzano, G. Molinié, A. Montani, G. Nord, M. Nuret, K. Ramage, W. Rison, O. Roussot, F. Said, A. Schwarzenboeck, P. Testor, J. Van Baelen, B. Vincendon, M. Aran, and J. Tamayo: HyMeX-SOP1: The Field Campaign Dedicated to Heavy Precipitation and Flash Flooding in the Northwestern Mediterranean, *Bull. Amer. Meteor. Soc.,* **95**, 1083–1100, https://doi.org/10.1175/BAMS-D-12-00244.1, 2014.

ECMWF, European Centre for Medium-Range Weather Forecasts (ECMWF) 15-year re-analysis (ERA-15) model data. NCAS British Atmospheric Data Centre, date of citation, http://catalogue.ceda.ac.uk/uuid/73ec447ea99457c77c0ef9692f76393f, 2006.

Sabine Griessbach, Lars Hoffmann, Reinhold Spang, Marc von Hobe, Rolf Müller, and Martin Riese, Infrared limb emission measurements of aerosol in the troposphere and stratosphere, Atmos. Meas. Tech., 9, 4399–4423, doi:10.5194/amt-9-4399-2016, 2016.

Hammann, E. and Behrendt, A.: Parametrization of optimum filter passbands for rotational Raman temperature measurements, Opt. Express, 23, 30767–30782, doi:10.1364/OE.23.030767, 2015.

Hauchecorne, A., M.-L. Chanin: Density and Temperature Profiles Obtained by Lidar Between 35 and 70 km, Geophysical Research Letters 7(8), 565-568, DOI: 10.1029/GL007i008p00565, 1980.

Hauchercorne, A., M.L.Chanin, P. Keckhout, and D. Nedeljkovic, Lidar monitoring of the temperature in the middle e lower atmosphere, Appl. Phys.B, 55, 29-34, 1992.

Dale F. Hurst Alyn Lambert William G. Read Sean M. Davis Karen H. Rosenlof Emrys G. Hall Allen F. Jordan Samuel J. OltmansValidation of Aura Microwave Limb Sounder stratospheric water vapor measurements by the NOAA frost point hygrometer, J Geophys Res Atmos. 2014 Feb 16;119(3):1612-1625. doi: 10.1002/2013JD020757, 2014.

Intergovernmental Panel on Climate Change (2007), Climate Change 2007: The Physical Science Basis. Contribution of Working Group I to the Fourth Assessment Report of the Intergovernmental Panel on Climate Change, edited by S. Solomon et al., 996 pp., Cambridge Univ. Press, Cambridge, U. K.

Leblanc, T., I. S. McDermid, A. Hauchecorne, and P. Keckhut, Evaluationof optimization of lidar temperature analysis algorithms using simulateddata, J. Geophys. Res., 103, 6177 – 6187, 1998a.

Leblanc, T., I. S. McDermid, C. Y. She, D. A. Krueger, A. Hauchecorne, and P. Keckhut, Temperature climatology of the middle atmosphere from long-term lidar measurements at mid- and low-latitudes, *J. Geophys. Res.,* 103., 17,191-17,204, 1998b.

Leblanc, T., I. Stuart McDermid, and Robin A. Aspey: First-Year Operation of a New Water Vapor Raman Lidar at the JPL Table Mountain Facility, California. Journal of Atmospheric and Oceanic Technology, Vol. 25, Iss. 8, pp. 1454-1462, 2008.

Leblanc, T., S. McDermid, Water Vapor Raman Lidar Measurements from the Ground to the Stratosphere: NDACC Implementation and the MOHAVE 2009 Validation Campaign, 2010.

Leblanc, T., McDermid, I. S., and Walsh, T. D.: Ground-based water vapor raman lidar measurements up to the upper troposphere and lower stratosphere for long-term monitoring, Atmos. Meas. Tech., 5, 17–36, https://doi.org/10.5194/amt-5-17-2012, 2012.

Li, T., T. Leblanc, and I. S. McDermid, Interannual Variations of Middle Atmospheric Temperature as Measured by the JPL Lidar at Mauna Loa Observatory, Hawaii (19.5^0N, 155.6^0W), *J. Geophysical Research, 113*, D14109,doi:10.1029/2007JD009764, 2008.

Lossow, S ., Khosrawi, F., Nedoluha, G. E., Azam, F., Bramstedt, K., Burrows, J. P., Dinelli, B. M., Eriksson, P., Espy, P. J., Maya García-Comas, John C. Gille, Michael Kiefer, Stefan Noël, Piera Raspollini, William G. Read, Karen H. Rosenlof, Alexei Rozanov, Christopher E. Sioris, Gabriele P. Stiller, Kaley A. Walker, and Katja Weigel: Comparison of H2O variability, Atmos. Meas. Tech., 10, 1111-1137, 2017.

Kantor, A.J. and Cole, A.E. Geofisica Pura e Applicata (1962) 53: 171. https://doi.org/10.1007/BF02007120.Macke, A., Seifert, P., Baars, H., Barthlott, C., Beekmans, C., Behrendt, A., Bohn, B., Brueck, M., Bühl, J., Crewell, S., Damian, T., Deneke, H., Düsing, S., Foth, A., Di Girolamo, P., Hammann, E., Heinze, R., Hirsikko, A., Kalisch, J., Kalthoff, N., Kinne, S., Kohler, M., Löhnert, U., Madhavan, B. L., Maurer, V., Muppa, S. K., Schween, J., Serikov, I., Siebert, H., Simmer, C., Späth, F., Steinke, S., Träumner, K., Trömel, S., Wehner, B., Wieser, A., Wulfmeyer, V., and Xie, X.: The

HD(CP)^2 Observational Prototype Experiment (HOPE) – an overview, Atmos. Chem. Phys., 17, 4887-4914, https://doi.org/10.5194/acp-17-4887-2017, 2017.

Marenco, F., di Sarra Alcide, Cacciani M., Fiocco G., and D. Fuà, Thermal structure of the winter middle atmosphere observed by lidar at Thule, Greenland, during 1993-1994, Journal of Atmospheric and Solar-Terrestrial Physics, 59, 151-158, 1997.

Pilins, C., Pandis, S. N., Seinfeld, J. H.: Sensivity of a direct climate forcing by atmospheric aerosols size and compositio, J. Grophys. Res., 100, 18739-18754,1995.

Rabier, Florence, Nadia Fourrié , D. Chafai, P. Prunet, Channel selection methods for Infrared Atmospheric Sounding Interferometer radiances Q. J. R. Meteorol. *Soc.* 128, 1011–1027, 2002. Riese, M., Ploeger, F., Rap, A., Vogel, B., Konopka, P., Dameris, M.,and Forster, P.: Impact of uncertainties in atmospheric mixing on simulated UTLS composition and related radiative effects, J. Geophys. Res., 117, D16305, doi:10.1029/2012JD017751, 2012.

Rosen, J.M., The boiling point of stratospheric aerosols, J. Appl. Meteorol., , 10, 1044–1046, 1971.

Serio, C., Masiello, G., Esposito, F., Di Girolamo, P., Di Iorio, T., Palchetti, L., Bianchini, G., Muscari, G., Pavese, G., Rizzi, R., Carli, B., Cuomo, V.: Retrieval of foreign-broadened water vapor continuum coefficients from emitted spectral radiance in the H2O rotational band from 240 to 590 cm^{-1}, Optics Express, vol. 16/20, 15816-15833, ISSN: 1094-4087, doi: 10.1364/OE.16.015816, 2008.

Sica, R. J., Sargoytchev, S., Argall, P. S., Borra, E. F., Girard, L., Sparrow, C. T., and Flatt, S.: Lidar measurements taken with a large-aperture liquid mirror. 1. Rayleigh-scatter system, Appl. Opt., 34 (30), 6925-6936, 1995.

D. Siméoni, C. Singer, G. Chalon: Infrared atmospheric sounding interferometer, Acta Astronautica, 40, 113-118, 1997.

Thorne, P. W., Parker, D. E., Christy, J. R., Mears, C. A.: Uncertainties in Climate Trrends, Lessons from Upper-Air Temperature Records, BAMS, 1437-1442, 2005.

Ugolnikov, O. S., Maslov, I. A.:Investigations of the Background Stratospheric Aerosol Using Multicolor Wide-Angle Measurements of the Twilight Glow Background, Cosmic Research, 56 (2), 85-93, 2018.

Uppala, S. M., P. W. KÅllberg, A. J. Simmons, U. Andrae, V. Da Costa Bechtold, M. Fiorino, J. K. Gibson, J. Haseler, A. Hernandez, G. A. Kelly, X. Li, K. Onogi, S. Saarinen, N. Sokka, R. P. Allan, E. Andersson, K. Arpe, M. A. Balmaseda, A. C. M. Beljaars, L. Van De Berg, J. Bidlot, N. Bormann, S. Caires, F. Chevallier, A. Dethof, M. Dragosavac, M. Fisher, M. Fuentes, S. Hagemann, E. Hólm, B. J. Hoskins, L. Isaksen, P. A. E. M. Janssen, R. Jenne, A. P. Mcnally, J.-F. Mahfouf, J.-J. Morcrette, N. A. Rayner, R. W. Saunders, P. Simon, A. Sterl, K. E. Trenberth, A. Untch, D. Vasiljevic, P. Viterbo, J. Woollen: The ERA-40 re-analysis". Quarterly Journal of the Royal Meteorological Society. **131** (612): 2961. doi:10.1256/qj.04.176, 2005.

U.S.Standard Atmosphere, Document ID: 19770009539, Accession Number: 77N16482, Report Number: NASA-TM-X-74335, NOAA-S/T-76-1562, NASA, 1976.

Vomel, H., Selkirk, H., Miloshevich, L., Valverde-Canossa, J., Valdes, J., Kyro, E., Kivi, R., Stolz, W., Peng, G., and Diaz, J. A.: Radiation dry bias of the Vaisala RS92 humidity sensor, J. Atmos. Oceanic Technol., 24, 953-963, 2007.

Whiteman, D. N.: Examination of the traditional Raman lidar technique. I. Evaluating the temperature-dependent lidar equations, Appl. Opt., 42, 2571-2592, 2003.

Whiteman, D. N., Melfi, S. H., and Ferrare, R. A.: Raman lidar system for the measurement of water vapor and aerosols in the Earth's atmosphere, Appl. Opt. **31**(16), 3068–3082 (1992).

Whiteman, D. N., B. Demoz, P. Di Girolamo, J. Comer, I. Veselovskii, K. Evans, Z. Wang, D. Sabatino, G. Schwemmer, B. Gentry, R. Lin, A. Behrendt, V. Wulfmeyer, E. Browell, R. Ferrare, S. Ismail, J. Wang (2006). Raman Lidar Measurements during the International H2O Project. Part II: Case Studies. Journal of Atmospheric and Oceanic Technology, vol. 23, p. 170-183, ISSN: 0739-0572, doi: 10.1175/JTECH1839.1, 2006.

Whiteman, D. N., Cadirola, M., Venable, D., Calhoun, M., Miloshevich, L., Vermeesch, K., Twigg, L., Dirisu, A., Hurst, D., Hall, E., Jordan, A., and Vömel, H.: Correction technique for Raman water vapor lidar signal-dependent bias and suitability for water vapor trend monitoring in the upper troposphere, Atmos. Meas. Tech., 5, 2893–2916, https://doi.org/10.5194/amt-5-2893-2012, 2012.

Wulfmeyer and Feingold, On the relationship between relative humidity and particle backscattering coefficient in the marine boundary layer determined with differential absorption lidar, J. Geophys. Res., 105. Vol. 104 , No. D4, p.4729 (1999JD901030), 2000.

Wulfmeyer, V., Behrendt, A., Bauer, H. S., Kottmeier, C., Corsmeier, U., Blyth, A., Craig, G., Schumann, U., Hagen, M., Crewell, S., Di Girolamo, P., Flamant, C., Miller, M., Montani, A., Mobbs, S., Richard, E., Rotach, M. W., Arpagaus, M., Russchenberg, H., Schlüssel, P., König, M., Gärtner, V., Steinacker, R., Dorninger, M., Turner, D. D., Weckwerth, T., Hense, A., Simmer, C.: Research campaign: The convective and orographically induced precipitation study - A research and development project of the World Weather Research Program for improving quantitative precipitation forecasting in low-mountain regions, Bulletin of the American Meteorological Society, 89, 1477-1486, ISSN: 0003-0007, doi: 10.1175/2008BAMS2367.1, 2008.

Zhao, J., Chu, X., Chen, C., Lu, X., Fong, W., Yu, Z., Jones, R. M., Roberts, B. R., and Dörnbrack, A.: Lidar observations of stratospheric gravity waves from 2011 to 2015 at McMurdo (77.84°S, 166.69°E), Antarctica: 1. Vertical wavelengths, periods, and frequency and vertical wave number spectra, J. Geophys. Res. Atmos., 122, 5041-5062, doi:10.1002/2016JD026368, 2017.